UNIVERSITÀ DEGLI STUDI DI PADOVA

Dipartimento di Fisica e Astronomia "Galileo Galilei"

Master Degree in Physics

Final Dissertation

First-principle study of a vdW material: TiS$_2$

Thesis supervisor

Prof. Pier Luigi Silvestrelli

Thesis co-supervisor

Dr. Alberto Ambrosetti

Candidate

Matteo Ricci

Academic Year 2018/2019

Abstract

Van der Waals (vdW) solids have attracted great attention since the discovery of graphene, with the essential feature being the weak *interlayer* bonding. The nature of these weak interactions is decisive for many extraordinary properties, but it is a strong challenge for current theory to accurately model long-range electron correlations. Nowadays, Titanium disulfide, TiS_2, which is an archetypal vdW solid, is receiving considerable attention. In fact, recent experimental analysis of chemical bonding in TiS_2, based on synchrotron X-ray diffraction data, allowed to obtain an accurate profile of the electron density in this material.

Comparison with available theoretical electron-density calculations, based on the Density Functional Theory (DFT), shows that, while a quantitative agreement is observed for the chemical bonding description in the covalent TiS_2 slabs, significant differences are instead identified for the *interlayer* interactions. In fact, the experiments reveal more electron deformation than theory, thus suggesting than the *interlayer* interactions are significantly stronger than the current theoretical description predicts.

In order to shed light on this discrepancy and to obtain a complete theoretical description of TiS_2, the Quantum Espresso first principles package, based on the DFT, is applied, by adopting various theoretical schemes to consider, at different levels, the vdW interactions also including the most recent developments. Several first principles simulations are carried out to evaluate structural, electronic and energetic properties of the system. In particular, we obtain the electron density distributions which can be directly compared with experimental data. Careful data analysis allows to get a better knowledge of TiS_2 properties and also to assess the quality of the newest theoretical approaches.

Employing some of the most popular DFT functionals, we reach reasonably satisfactory agreements with experimental data, both for structural and electronic properties.

Moreover, we propose a tuning of the q parameter in the original vdW-DF functional of Hamada, obtaining a value of the charge density at the bond critical point in the S-S *interlayer* fragment, in better agreement with experimental data.

Contents

Chapter 1

Introduction

There are a large number of materials with mild stiffness, which are not as soft as tissues and not as strong as metals. These semihard materials include energetic materials, molecular crystals, layered materials, and vdW crystals. The integrity and mechanical stability of these materials are mainly determined by the interactions between instantaneously induced dipoles, the so called London dispersion force or van der Waals force.

Layered van der Waals (vdW) materials have unique properties, and these two-dimensional solids are central to current research in solid-state science. Although graphite is probably the most widely known layered material, nowadays transition metal dichalcogenides (TMDs) are attracting much attention due to a range of exciting applications, including electrode materials for ion batteries [1] , thermoelectrics [2] , catalysis [3] , topological insulators [4] , superconductors [5] , and charge-density-wave materials [6]. In addition, single layers of TMDs are available due to the weak *interlayer* interaction [7] .

Mono- and few-layer TMDs have unique properties which cannot appear in the bulk [8] , and heterostructures built layer by layer using different materials have entirely new properties [9] . In all the numerous fundamental and applied investigations of vdW materials, the weak *interlayer* interactions play a central role in the formation, intercalation, exfoliation and layer-by-layer building of the materials as well as being decisive for their unique properties.

In TMDs, a transition metal atom (M) layer is sandwiched by two chalcogen atom (X) layers. It is commonly assumed that the MX_2 slabs are stacked by vdW interactions, whereas the intralayer M–X interactions are covalent. The *interlayer* part of the structure is typically referred to as the vdW gap. In the condensed-matter field, the vdW term is used typically for London dispersion forces, which are caused by instantaneously induced dipoles [10].

The quasi two-dimensional nature of MX_2 compounds gives rise to a marked anisotropy in transport properties. The most important feature, however, is that the weak *interlayer* bonding permits the intercalation of various guests between the layers. Depending on the guest species, unsual and dramatic changes in the physical properties of the host can occur, and this feature has stimulated much research interest on these materials.

The strength of the *interlayer* interaction affects not only the binding and exfoliation energy of the layers, but also the electronic properties. A combined high-pressure X-ray diffraction and vdW-modified DFT study of SnS_2 , which is isostructural with TiS_2, showed that the *interlayer* bonding strength significantly influences the electronic structure, including the band-gap [11] but standard (no vdW) and vdW-corrected DFT calculations show different electronic properties due

to differences in the strength of the *interlayer* interaction [12]: this example makes clear that a precise description of the weak *interlayer* interactions is vital for theoretical predictions of the physical properties of these materials.

One of the most important quantity to study in solid state physics is the electron density (ED) of a given crystal. It probably represents the most information-rich observable available since it has become possible to determine EDs from analysis of structure factors obtained from accurate X-ray diffraction data. X-ray ED investigations is used to study chemical bonding in a wide range of materials.

During the past decade, the accuracy of experimental X-ray diffraction data has increased dramatically owing to the use of high-energy synchrotron sources, which significantly limit systematic errors in the data and, thanks to these modern techniques, nowdays it is possible to evaluate structural, vibrational, energetic and electronic properties of a wide range of a material in an extremely accurately way.

Because of this high-level development of the experimental side, it is increasingly challenging for the theoretical models to accurately predicts the structural and mechanical properties of these semihard materials, especially in the frame of DFT, where the non-local exchange correlation functionals are not well known.

Titanium disulfide is a solid whose electronic structure is also nowdays quite disputed, because the properties observed could be interpreted in terms of metallic, semimetallic and extrinsic semiconductor models, even if some experimental evidences have shown that TiS_2 is an extrinsic semiconductor [13].

There is a considerable technological interest in TiS_2 as a host material for intercalation reactions with alkali metals. In particular, it was the typical intercalation cathode material used in early Li-ion batteries, and it is still considered a candidate, for example, for high-power applications or all-solid-state batteries [14].

TiS_2 has also received attention as an oxygen catalyst for fuel cells [15], as a catalyst for the preparation of urethanes [16] and linear polyesters [17], as a catalyst in the thermal transformation of dodecacarbonyltriiron ($Fe_3(CO)_{12}$) [18], and as a solid lubricant [19].

Nowdays, this archetypal vdW solid is receiving considerable attention. In fact, recent experimental analysis of chemical bonding in TiS_2, based on synchrotron X-ray diffraction data [20], allowed to obtain an accurate profile of the electron density in this material.

Comparison with available theoretical electron-density calculations, based on DFT, shows that, while a quantitative agreement is observed for the chemical bonding description in the covalent TiS_2 slabs, significant differences are instead identified for the *interlayer* interactions. In fact, the experiments reveal more electron deformation than theory, thus suggesting than the *interlayer* interactions are significantly stronger than the current theoretical description predicts.

At this point, the question that naturally arises, is if the current theoretical approaches are inappropriate to correctly describe these vdW materials, like TiS_2.

The main purpose of this thesis work is to shed light on this discrepancy. We have applied the Quantum Espresso [21] DFT packages to include, at different levels, vdW interactions in our ab-initio calculations, also to assess the quality of some of the newest theoretical approaches.

Chapter 2

Methods

In this chapter a theoretical overview of the Density Functional Theory (DFT) is made, with particular emphasis on its use as a framework for ab initio calculations. We also mention and describe vdW effects in condensed matter physics and, finally, we focus on the most recent DFT developments, showing different approaches to deal with vdW interactions at different levels.

2.1   The Density Functional Theory

Density functional theory (DFT) is a computational quantum mechanical modeling method used in physics, chemistry and, in general, in materials science, to investigate the electronic structure (principally the ground state) of many-body systems, in atoms, molecules, and condensed phases. Using this theory, the properties of a many-electron system can be determined by using functionals of the electron density. DFT is certainly the most popular and versatile methods available in condensed-matter physics, computational physics, and computational chemistry.

In the context of computational materials science, ab-initio DFT calculations allow the prediction and calculation of material behavior on the basis of quantum mechanical considerations. In principle the calculation is exact and the only ingredients needed are the number and the types of involved atoms. In practice, a number of approximations are introduced, as described in the following.

Let us consider a many-body quantum system made of N nuclei and M electrons interacting via the Coulomb potential. Let be the electron mass m_e, the electron charge e, the ions masses M_I and the ion chargees $Z_I e$: in this way the full Hamiltonian operator of the system, expressed in atomic units, reads

$$H = \sum_{i=1}^{M} -\frac{\nabla_i^2}{2} + \sum_{I=1}^{N} -\frac{\nabla_I^2}{2M_I} + \frac{1}{2}\sum_{i\neq j}^{M} \frac{1}{|\vec{r_i} - \vec{r_j}|} + \frac{1}{2}\sum_{I\neq J}^{N} \frac{Z_I Z_J}{|\vec{R_I} - \vec{R_J}|} - \sum_{I,i}^{N,M} \frac{Z_I}{|\vec{r_i} - \vec{R_I}|}$$

the solution of the time-independent problem is given by the many body Schröedinger equation:

$$H \ \Psi(\vec{r}, \vec{R}) = \ E \ \Psi(\vec{r}, \vec{R}) \tag{2.1}$$

where $\Psi(\vec{r}, \vec{R})$ is the wavefunction of the entire system and the pair $(\vec{r}, \vec{R})$ contains all the spatial coordinates of the electrons and of the nuclei respectively.

It is well known that such a many body quantum problem is not exactly analytically solvable and hence the need to an alternative approach to solve this wide class of problems.

The purpose of this section is to develop a theoretical overview of the main conceptual steps that allow us to arrive at the DFT formulation of the many-body problem mentioned above.

First of all, we can observe that the order of magnitude of the ratio between a typical nuclear mass and the electron mass is $\frac{m}{M_I} \approx \frac{1}{10^4}$ and this means that the nuclear dynamics occurs on different energetic and temporal scale with respect to the ones associated to the electrons. As a consequence, we can decouple nuclear and electronic motion within the so called Born-Oppenheimer (BO) approximation.

The basic idea on which this approach is built, is to observe that the nuclear dynamics is not affected by quantum effects because the typical thermal wavelenght of the nucleus at room temperature is much smaller than the typical interatomic distance a_0:

$$\lambda_I^{(T)} = \frac{1}{6\pi M_I K_b T_r} << a_0$$

where T_r is the room temperature and K_b is the Boltzmann constant.

If the above condition yields, the nuclei evolve according to the Newton's law and so the many-body problem can be formulated in the following way

$$(T_e + V_{ee} + V_{en} + V_{nn}) \ \psi_e(\vec{r}, \vec{R}) = \epsilon(\vec{R}) \ \psi_e(\vec{r}, \vec{R})$$

$$[T_n + \epsilon(\vec{R})] \ \Phi(\vec{R}) = \ E \ \Phi(\vec{R}) \rightarrow M\frac{d^2 R}{dt^2} = -\frac{\partial \ \epsilon(\vec{R})}{\partial(\vec{R})}$$

where T_e and T_n are respectively the nuclear and electronic kinetic operators, V_{nn} is the nucleus-nucleus Coulombian repulsion and V_{en} denotes the electron-nucleus Coulombian attraction.

The first equation represents the Schröedinger equation of the electrons in presence of the nuclei and the associated eigenvalue $\epsilon(\vec{R})$, that appears in the second equation, is a potential that affects the classical dynamics of the nuclei.

In this spirit, the lowest order approximation is to consider the nuclei as fixed on their equilibrium positions: in this way the only contributions due to the nuclear presence in the system appear in the first equation within the terms V_{nn} and V_{en}.

Within the BO approximation, the strategy to solve our many body quantum problem is the following:

- The first step is the resolution of the Schröedinger equation for the electronic Hamiltonian: this allow us to find $\epsilon(\vec{R})$.

- Once $\epsilon(\vec{R})$ is computed, the second equation can be solved and this will give us the nuclear kinetic energy T_n and the forces acting on the nuclei.

- With the knowledge of both $\epsilon(\vec{R})$ and T_n, it is possible to compute the energy of our many body system as $E = T_n + \epsilon(\vec{R})$ and an approximation of the exact wave function will be $\Psi(\vec{r}, \vec{R}) = \Phi(\vec{R})\psi_e(\vec{r}, \vec{R})$.

Since the first conceptual step means to solve the electronic many body problem, the obvious question that arises now is how to determine the wavefunction $\psi_e(\vec{r})$.

The answer is given by Hohenberg-Khon (HK) theorems [22], the main tools on which DFT is based.

As before, let us consider a system made of M electrons supposing that all the nuclei are fixed in their equilibrium position ($T_n = 0$) and let us also assume that the system is in its non-degenerate ground state (GS): in this situation all the M electrons are moving in an external potential that is generated by the nuclear static charges.

The electron density operator can be written as

$$n(\vec{r}) = \sum_{i=1}^{M} \delta(\vec{r} - \vec{r}_i)$$

It is immediate to show that the GS electronic particle density has the following expression:

$$n_0(\vec{r}) = \int d\vec{r_1}...d\vec{r_M} \ \psi_{e(0)}^*(\vec{r_1}, ..., \vec{r_M})\psi_{e(0)}(\vec{r_1}, ..., \vec{r_M})$$

The meaning of the above equation is that one can associate a single-particle density function $n_0(\vec{r})$ to the GS electronic many-body wavefunction $\psi_{e(0)}$.

At this point is clear that, in order to compute n_0, one has to know $\psi_{e(0)}$, that is a strongly complicated object.

The HK theorems, applicable to any system consisting of electrons moving under the influence of an external potential, allow us to give a solution to such an apparently unsolvable problem.

- The first HK theorem states that, once the external potential is fixed, the electronic ground state wavefunction is a unique functional of the ground state density:

$$\boxed{\psi_{e(0)} = \psi_e\left[n_0(\vec{r})\right]}$$

as a corollary, also the ground state total energy of the system will be a unique functional of n_0:

$$E_0 = E\left[n_0(\vec{r})\right] = \langle \psi_e\left[n_0\right]| V_{ee} + V_{en} + T_e |\psi_e\left[n_0\right]\rangle$$

- The second HK theorem guarantees that the variational principle holds for the energy functional written above:

$$\boxed{\min\{E\left[n(\vec{r})\right]\} = E\left[n_0(\vec{r})\right] = E_0}$$

this means that a successful minimization will yield the ground-state density and, consequently, all the other ground-state observables.

The crucial point is that, once the number of electrons and the external potential are fixed, the other terms such as V_{ee} and T_e will be the same for all the system with M electrons and so, all the system with the same number of electrons under the influence of the same external potential, will have the same ground state density.

This suggests to map the system with M electrons interacting via the real potentials onto a fictitious and non-interacting system whereby the electrons move within an effective single-particle potential.

In this way one can write down the equations for a new system in which, according to the HK theorems, the ground state density $n_0(\vec{r})$ is exactly the same as that the real system.

In particular, one can solve the so called Kohn–Sham (KS) equations for the auxiliary and non-interacting system in which an effective single-particle external potential $V_{eff}(\vec{r})$ appears. In this framework, the KS equations read

$$\left[-\frac{\nabla^2}{2} + V_{eff}(\vec{r})\right]\phi_i(\vec{r}) = \epsilon_i\phi_i(\vec{r}) \quad i = 1, ..., M \tag{2.2}$$

where the orbitals ϕ_i, according to HK theorems, reproduce the density $n(\vec{r})$ of the original many-body system

$$n(\vec{r}) = \sum_{i=1}^{M}|\phi_i(\vec{r})|^2 \ . \tag{2.3}$$

The term $V_{eff}(\vec{r})$ in (2.2) is the sum of the following terms:

$$V_{eff}(\vec{r}) = V(\vec{r}) + \int d\vec{r'}\frac{n(\vec{r'})}{|\vec{r} - \vec{r'}|} + V_{XC}[n(\vec{r})] \tag{2.4}$$

Here, $V(\vec{r})$ denotes the nuclear contribution to the external potential that affects all the fictitious free electrons. The integral term is the Hartree term, describing the electron-electron Coulomb repulsion and, finally, there is the so called "exchange-correlation functional", that is $V_{XC}[n(\vec{r})]$. It is common to split this last term into a sum of two factors:

$$V_{XC}[n(\vec{r})] = V_X[n(\vec{r})] + V_C[n(\vec{r})]$$

In this expression the first factor is the exchange energy functional, in which the effects coming from the antisymmetry of fermionic wavefunctions are accounted. The second term is the correlation functional and takes into account all the beyond-Hartee-Fock correlation effects.

The Kohn-Sham equations in (2.2) are so far exact: no approximations have been made because we have simply mapped the fully interacting system onto an auxiliary and non-interacting system, that yields the same GS density. Unfortunately, the exact expression of the exchange-correlation functional in term of the electronic density $n(\vec{r})$ is not known, except for the free electron gas, and, for this reason, the major problem with DFT is to compute V_{XC} through the use of some suitable approximations.

Now we will discuss more in detail the most popular approaches to include the exchange and correlation effects in quantum ab initio DFT calculations.

2.1.1 The Exchange-Correlation Energy Functional

It is useful to start by expressing the KS equation in terms of functionals of the electronic density [23]

$$E_{KS}[n(\vec{r})] = T_{KS}[n(\vec{r})] + \int d\vec{r}\, n(\vec{r}) V(\vec{r}) + \int d\vec{r} d\vec{r}' \frac{n(\vec{r}) n(\vec{r}')}{|\vec{r} - \vec{r}'|} + E_{XC}[n(\vec{r})] \qquad (2.5)$$

where, through the use of eq. (2.3), one can write

$$T_{KS}[n(\vec{r})] \rightarrow T_{KS}[\phi(\vec{r}), \phi^*(\vec{r})] = \sum_{i=1}^{M} \int d\vec{r} \frac{1}{2} |\nabla \phi_i(\vec{r})|^2$$

T_{KS} does not represent the true kinetic energy of the system, but is instead the exact kinetic energy of a non-interacting system.

The KS equations in their usual form can be obtained from the minimization of (2.5), with the constraint $N = \int d\vec{r}\, n(\vec{r})$.

The relation between V_{XC} and E_{XC} is

$$V_{XC}(\vec{r}) = \frac{\delta E_{XC}[n(\vec{r})]}{\delta n(\vec{r})}$$

which yields:

$$\frac{\delta E_{XC}[n(\vec{r})]}{\delta n(\vec{r})} = \frac{\delta}{\delta n(\vec{r})} \int d\vec{r}\, n(\vec{r})\, \epsilon_{XC}[n(\vec{r})] =$$

$$\frac{\partial}{\partial n(\vec{r})} \left[n(\vec{r}) \epsilon_{XC}[n(\vec{r})] \right] \rightarrow$$

$$V_{XC} = \epsilon_{XC}[n(\vec{r})] + n(\vec{r}) \frac{\partial \epsilon_{XC}[n(\vec{r})]}{\partial n(\vec{r})}$$

That is the explicit expression of the exchange-correlation potential appearing in (2.2) in terms of energy density ϵ_{XC}.

The Local Density Approximation

One of the simplest approximations for the exchange correlation functional is the local-density approximation (LDA), where the functional depends only on the density at the position where the functional is evaluated and not, for example, on derivatives of the density.

The spirit of the approximation is in the fact that even if in a real system $n(\vec{r})$ is not uniform, one uses the $E_{XC}[n]$ expression of the homogeneous electron gas (HEG). This latter is a quantum mechanical model of interacting electrons in a solid where the positive charges (i.e. atomic nuclei) are assumed to be uniformly distributed in space and the electron density is a uniform quantity in space as well.

Usually, in LDA, the exchange correlation functional is expressed as the sum of the two contribution separately:

$$E_{XC}[n(\vec{r})] \ = \ E_X[n(\vec{r})] + E_C[n(\vec{r})] \tag{2.6}$$

The exchange term is still considered at the HF level of theory. In order to explain the physical nature of this contribution we can make a simplified -but useful- argument according to which we can image that the exchange term is the one that takes into account that an electron of a given spin will be surrounded by a region where the density of electrons with the same spin (say, $\uparrow$) is reduced.

Intuitively, the effect of this "exchange hole" can be estimated by considering a uniform density inside a sphere of typical radius r_0 and zero elsewhere and so, since the hole contains a single electron, one has immediately

$$r_s = (3/(4\pi n_\uparrow))^{1/3} \tag{2.7}$$

that defines the so called Wigner-Seitz parameter. In this spirit, computing the electrostatic energy density, one can recover the same dependence on density of the well known Dirac exchange term:

$$\epsilon_X^{HEG} = -\frac{3}{4}\left(\frac{3}{\pi}\right)^{1/3} n^{1/3} \tag{2.8}$$

and it immediately leads to the usual expression of the exchange density functional:

$$E_X^{LDA} = -\frac{3}{4}\left(\frac{3}{\pi}\right)^{1/3} \int d\vec{r}\, n(\vec{r})^{4/3} \tag{2.9}$$

The correlation energy, by definition, is not included at the HF level of theory, but is a fundamental part of the DFT.

Even for a HEG, a general explicit expression of the correlation energy is not available, except for the high- and low-density limits (HD and LD respectively).

In the HD limit, the correlation energy can be computed, for example, within the RPA (random phase approximation) [24], and then the dependence with respect to the Wigner-Seitz parameter introduced in (2.7) is the following:

$$\epsilon_C^{HD}(r_s) = A\,ln(r_s) + B + r_s(C\,ln(r_s) + D) \tag{2.10}$$

However, in general, a description of the correlation energy in a wide range of densities requires a suitable parameterization scheme, based on fitting functions to the near-exact Quantum Monte

Carlo (QMC) results of Ceperley and Alder [25]. Examples of correlation functionals obtained with this method are the Vosko-Wilk-Nusair [26], the Perdew-Wang [27] or the Perdew-Zunger [28] one. In particular, the former and the latter are the two parameterization of LDA functionals implemented in Quantum Espresso.

Some of these functional forms, such as the Vosko-Wilk-Nusair one, are usually analytically complicated and inherently contain numerical irregularities.

For completness we end the discussion on the LDA, by mention the local spin-density approximation (LSDA): this is a straightforward generalization of the LDA to include electron spin. In this more general apporach the exchange-correlation functional reads

$$\epsilon_{XC}^{LSDA}(n_\uparrow(\vec{r}); n_\downarrow(\vec{r})) = \int d\vec{r}\, n(\vec{r})\, \epsilon_{XC}[n_\uparrow(\vec{r}); n_\downarrow(\vec{r})] \qquad (2.11)$$

where $\epsilon_{XC}[n_\uparrow(\vec{r}); n_\downarrow(\vec{r})]$ is the exchange-correlation energy for a spin-polarized HEG. The aim of such a generalization of the LDA is in the description of spin system.

The LDA and LSDA are very successful approximation for many systems of interest, especially those where the eletronic density is quite uniform such as bulk metals, but also for less uniform systems such as molecules, semiconductors, and ionic crystals. There are, however, a number of features that the LDA fails to reproduce: the most dramatic being the following:

- The LDA has a tendency to overestimate the exchange energy and underestimate the correlation energy [29]. However, the errors in the evaluation of the exchange and correlation parts usually tend to compensate each other to a certain degree, leading to surprisingly good result in a wide range of systems.

- Electronic densities of atoms in the core region, where the electrons are strongly localized, is poorly described: the reason is that LDA fails to cancel the self-interaction, which is important for strongly localized states. To the other side, the electronic density in the valence region of the atom is much better reproduced, although it still decays into the vacuum with an incorrected behavior.

- Effects due to truly non local correlation effects, such as the vdW corrections, are not accounted within LDA.

The Generalized Gradient Approximation

To correct for the tendency of LDA to overestimate the exchange energy and underestimate the correlation one, a common strategy is to take into account the gradient of the density, because of the non-homogeneity of the true electron density of a given system: this allows for corrections based on the changes in density away from the considered space coordinate.
These schemes are the so called generalized gradient approximations (GGA)[30] and, in this framework, the exchange correlation functional is of semi-local type and has the following form

$$E_{XC}[n(\vec{r})] = \int d\vec{r}\, n(\vec{r})\, \epsilon_{XC}[n(\vec{r})]\, F_{XC}^{GGA}[s(\vec{r})] \tag{2.12}$$

Here $F_{XC}^{GGA}[s(\vec{r})]$ is the enhancement factor, where the variable $s(\vec{r})$ is the dimensionless reduced gradient, defined as:

$$s(\vec{r}) = \frac{1}{2\,(3\pi^2 n(\vec{r}))^{1/3}} \frac{|\nabla n(\vec{r})|}{n(\vec{r})} \tag{2.13}$$

The reduced gradient expresses how fast the density varies on the scale of the local Fermi wavelenght k_f.
It is important to point out that when $|\nabla n(\vec{r})| \to 0$, we have also $s(\vec{r}) \to 0$ and, with the constraint $F_{XC}^{GGA}[s(\vec{r}) \to 0] \to 1$, the LDA is recovered.
Unlike the LDA, there is no unique form for the GGA, and indeed many possible variations are possible, each corresponding to a different enhancement factor.
Using this approach, very good results for molecular geometries and ground-state energies have been achieved.
Taking into account the spatial variation of the electronic density, the GGA exhibits substantial improvements with respect to the first two deficiencies of LDA mentioned in the previous section. More specifically, the LDA usually tends to overestimate the binding energies, and, as a direct consequence, to underestimate bond lenghts in molecular system.
Potentially more accurate than the GGA functionals are the so called meta-GGA functionals, a natural development beyond the GGA. Meta-GGA DFT functional in its original form includes the second derivative of the electron density, while GGA, as said before, includes only the density and its first derivative.

Despite the considerable improvements, the GGA and meta-GGA fail, exactly as the LDA, in the description of non-local correlation effects. Since in a wide class of systems the mentioned effects are absolutely non-negligible, these DFT calculation appear to be inadequate.
Starting from LDA and GGA, new methods have been developed to better describe non-local correlation interactions.

2.2 VdW-Corrected Methods in DFT

Identified in 1873 [31], the vdW interaction, is a force that today attracts more interest than ever. It was first introduced in a doctoral thesis by Johannes Diderik van der Waals "on the continuity of the gaseous and liquid state" at Leiden University . The existence of the vdW force [32] is today well established. It is present everywhere, but its variation from one environment to another and its complex manifestations still pose challenging questions nearly one hundred years after van der Waals was awarded the Nobel Prize in physics. These questions are relevant for such varied systems as soft matter, surfaces, and DNA, and in phenomena as different as supramolecular binding, surface reactions, and the dynamic properties of water.
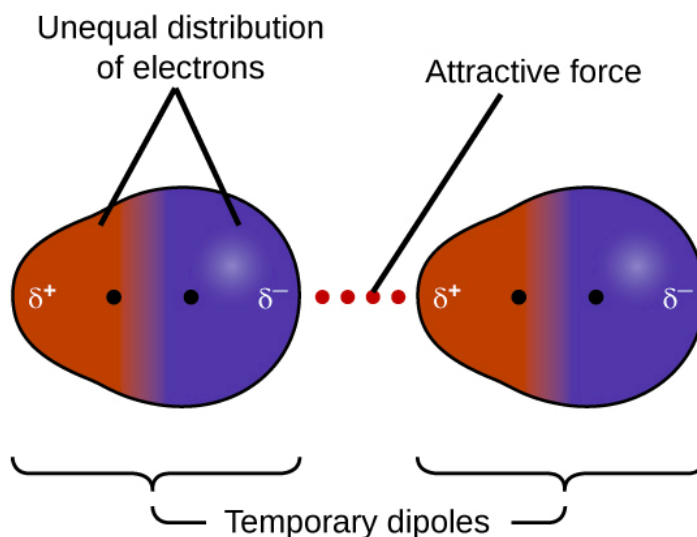

Figure 2.1: Instantaneously induced dipole, source of London dispersion forces.

In physical-chemistry terminology, the possible sources of the vdW interaction are considered to be the following

- Two permanent dipoles (Keesom force).

- A permanent dipole and a corresponding induced dipole (Debye force).

- Two instantaneously induced dipoles (London dispersion force) [33].

In the condensed-matter community, instead, typically just the last situation mentioned, which is a pure quantum phenomenon, is considered the real source of vdW interactions.

A proper theory for atoms and molecules should account for all forces at play, including covalent bonds, hydrogen bonds, and electrostatic interactions, because such combinations of interactions are relevant in typical materials and systems: DFT represents such a general framework.

Like all non-relativistic electronic effects, the vdW interactions are present in the exact DFT exchange-correlation functional, but as discussed before, vdW effects are not properly described by standard approximate DFT schemes.

The field of vdW interactions in DFT was practically absent before around 1990, but picked up at the end of the previous century, grew immensely during the first decade of the present one, and increased exponentially thereafter.

Overall, there are now several kinds of approaches to include vdW interaction in DFT calculations. Several of these are based on computing atom-based pair potentials and adding an empirical damped dispersion correction (see for example ref. [34]), instead others are built on a non-local exchange-correlation density functional, such as those proposed by Vydrov and Van Voorhis [35]. In this section we will discuss the vdW corrections, at different levels, adopted in this work.

2.2.1 GGA + Grimme-D2

This method [34] represents a development of its original version, Grimme-D1 (GD1) [36], named also DFT-D. This, as its more recent version, is an empirical method to account for vdW interactions in practical DFT calculations. In this approach a semi-local exchange-correlation functional (i.e. GGA) is adopted; this choice, as it was pointed out before, does not properly include vdW effects, since these are of non-local nature.

In its application GD1 has shown different shortcomings [34], the main ones can be summarized as follows, which are overcome by GD2:

- Consistent atomic parameters (C_6 coefficients) are only available for elements H, C–Ne, but studies of supramolecular structures or problems in material science require parameters for elements from the whole periodic table.

- Test calculations for molecules with third-row elements of the periodic table, showed systematic errors.

- Adding the dispersion energy to the standard GGA DFT energy leads to inconsistencies for "normal" thermochemistry (e.g. atomization energies: the dispersion correction is zero for the free atom and always nonzero (and large) for the molecule).

The inclusion of London dispersion correction with Grimme-D2 (GD2) is made in a post-processed way: once the energy of the system is computed within the GGA, an empirical damped contribution that takes into account for the vdW corrections is added

$$E = E_{GGA} + E_{GD2} \qquad (2.14)$$

The vdW correction has the following form:

$$E_{GD2} = S_6 \sum_{i=1}^{N_{at}-1} \sum_{j=1+1}^{N_{at}} \frac{C_6^{ij}}{R_{ij}^6} f_d(R_{ij}) \qquad (2.15)$$

Where, N_{at} is the number of atom in the system, R_{ij} is the interatomic distance, $C_6^{ij} = \sqrt{C_6^i C_6^j}$ denotes the dispersion coefficient for atom pair ij and S_6 is a global scaling factor that depends only on the DF used: in our case GD2 is coupled with a DF in GGA (PBE [37]) and so $S_6 = 0.75$. More specifically, it is important to underline a limiting factor of this approach: the values for the coefficient C_6^i are tabulated for each element of the periodic table and they are insensitive to the particular chemical situation (for instance, C_6^C for carbon in methane takes exactly the same value as that for the one in benzene within this approximation, although the environment of the C atom is different).

f_d is a damping function whose role is to avoid short-range divergences and double counting

of correlation-energy contributions. The analytic expression of such a damping function is the following:

$$f_d(R_{ij}) = \frac{1}{1 + e^{-d(R_{ij}/R_r^{ij} - 1)}} \tag{2.16}$$

Here, d denotes the damping factor and $R_r^{ij} = R_r^i + R_r^j$ is another tabulated parameter with the same limitations of C_6^{ij}.

2.2.2 GGA + Grimme-D3

This method represents an improved version of the previous one. The philosophy on which the method is constructed is the same as before but, unlike GD2, GD3 has more flexibility to adapt itself to predict vdW effects in several systems.
Also in this case the total energy reads:

$$E = E_{GGA} + E_{GD3} \tag{2.17}$$

where

$$E_{GD3} = -\sum_{i=1}^{N_{at}} \sum_{j=i+1}^{N_{at}} \left(f_{d,6}(R_{ij}) \frac{C_6^{ij}}{R_{ij}^6} + f_{d,8}(R_{ij}) \frac{C_8^{ij}}{R_{ij}^8} \right) \tag{2.18}$$

The main difference between this method and the one presented above is that here, in addiction to C_6^{ij}, the higher order C_8^{ij} coefficient is present, and, more importantly, both these coefficients are geometry-dependent, in such a way to be adjusted on the basis of the local environment (coordination number) around atoms i and j.
The damping functions $f_{d,n}$ have the following expression:

$$f_{d,n}(R_{ij}) = \frac{S_n}{1 + 6\,(\,R_{ij}\,/\,R_r^{ij})^{-\alpha_n}} \tag{2.19}$$

where $R_r^{ij} = \sqrt{\dfrac{C_8^{ij}}{C_6^{ij}}}$, the parameters α_6, α_8 and S_6 are fixed respectively to 14, 16 and 1 and S_8
is adjusted on the basis of the choice of the exchange-correlation functional.
Although their high level accuracy for the description of a wide class of physical and chemical processes, robustness, applicability to all kinds of systems (from molecules to condensed bulk phases) and fast computational time, these semi-local DF approaches are inadequate to describe many different cases, particularly extended systems.
Therefore the need arises to introduce truly non local exchange-correlation functionals that are able to account accurately for vdW corrections. Two of the most popular methods used in recent first-principle studies based on non local exchange-correlation functionals, are presented in the following two subsections.

2.2.3 rVV10

rVV10 [35] (revised Vydrov and Van Voorhis) belongs to the class of functional designed to minimize the error of the binding energies and interaction energies curves in a certain collection of materials, such as the S22 data set [38] made of molecular dimers, aiming for a general use for all materials.

In this scheme the exchange energy is computed within the GGA (2.12), as it was described in the previous section.

The correlation energy contribution really includes non-local effects and has the following form:

$$E_C^{rVV10} = \int d\vec{r}\, n(\vec{r}) \left[\frac{1}{32} \left(\frac{3}{b^2} \right)^{3/4} + \frac{1}{2} \int d\vec{r'}\, n(\vec{r'})\, \Phi(\vec{r};\vec{r'}) \right] \tag{2.20}$$

where $\Phi(\vec{r},\vec{r'})$ is the non local correlation kernel (NLCK) (i.e. it depends on two different radius vector: $\vec{r}$ and $\vec{r'}$). More specifically, the expression of the rVV10 NLCK is the following

$$\Phi = -\frac{3}{2}(k\,k')^{-3/2} \left[\frac{g\,g'}{k\,k'} \left(\frac{g}{k} + \frac{g'}{k'} \right) \right]^{-1}$$

$$g = \omega_0\, |\vec{r} - \vec{r'}|^2 + k$$

$$\omega_0 = \sqrt{ c \left| \frac{\nabla n(\vec{r})}{n(\vec{r})} \right|^4 + \frac{4\pi}{3} n(\vec{r}) }$$

$$k = \frac{3\pi b}{(576\pi)^{1/6}} n(\vec{r})^{1/6}$$

where the primed varibles g' and k' are referred to the electronic density computed on point $\vec{r'}$.

In the original version, namely VV10, the values of the two empirical parameters b and c optimized by Vydrov and Van Voorhis were found to be $b = 5.9$ and $c = 0.0093$, respectively. In the revisited version, Sabatini and coworkers made the approach more efficient [39], retaining the value of c and optimizing b with respect to the S22 data set, finding $b = 6.3$.

Comparing rVV10 to VV10 performances, one finds that VV10 tends to systematically underestimate the binding energy. Therefore, the slightly larger value of b proposed in the rVV10 helps to reduce the under-binding of the original method.

The functional dependence of the NLCK is

$$\Phi(\vec{r},\, \vec{r'}) \leftrightarrow \Phi(n(\vec{r}),\, n(\vec{r'}),\, \nabla n(\vec{r}),\, \nabla n(\vec{r'}),\, |\vec{r} - \vec{r'}|)$$

If the kernel depends separately on densities and gradients in the two points, the double integral appearing in (2.20) is a 6-dimensional object, very expensive to compute, hence the need of an efficient intergation method.

Basically, the idea of rVV10 is to reduce the NLCK dependence on density and gradients at separately points $\vec{r}$ and $\vec{r'}$, to a dependence through a combined function of these arguments and to compute this integral in momentum space:

$$\Phi(n(\vec{r}),\, n(\vec{r'}),\, \nabla n(\vec{r}),\, \nabla n(\vec{r'}),\, |\vec{r} - \vec{r'}|) \rightarrow \Phi(q(n(\vec{r}), \nabla n(\vec{r}));\, q(n(\vec{r'}), \nabla n(\vec{r'});\, |\vec{r} - \vec{r'}|)$$

In this framework, one can pre-calculate the value of the kernel for a number of points in a 2D q-grid of 20×20 points in momentum space and interpolate in between following the procedure

proposed by G. Roman-Perez [40].

With its efficiency in predicting correctly structural, vibrational and electronical properties, rVV10 maintains the outstanding precision of the original VV10 in non-covalently bound complexes and performs well in representative covalent, ionic, and metallic solids.

2.2.4 vdW-DF Functionals

Within the DFT framework, the van der Waals density functionals vdW-DF [41],are a family of functionals able to reproduce both covalent and weak van der Waals (vdW) interactions in a seamless fashion

The exchange correlation energy E_{XC}, sum of exchange energy E_X and correlation energy E_C, is expressed as

$$E_{XC}^{vdW-DF} = E_X^{GGA} + E_C^{LDA} + E_C^{NL} \tag{2.21}$$

where E_X^{GGA} is of the same form of the one introduced in (2.12), E_C^{LDA} is the short-range correlation energy within the local density approximation and E_C^{NL} is the non local correlation energy.

The non local nature of vdW-DF methods is contained into this latter contribution, whose explicit expression could be written through a NLCK, in the same form of (2.20)

$$E_C^{NL} = \frac{1}{2} \int d\vec{r} \int d\vec{r'} \, n(\vec{r}) \Phi(d, d') n(\vec{r'}) \tag{2.22}$$

In this scheme, the NLCK depends on density and its gradients through the relations

$$d = q_0(n(\vec{r}), \nabla n(\vec{r})) |\vec{r} - \vec{r'}|$$
$$d' = q_0(n(\vec{r'}), \nabla n(\vec{r'})) |\vec{r} - \vec{r'}|$$

where q_0 determines the long-range asymptotic behavior, as well as the short-range damping of the NLCK Φ.

Ultimately, this choice implicitly implies that the only non-local correlation term is due to vdW interactions, where the vdW kernel is actually derived in a way to model dispersion interactions.

In general vdW-DF functionals give a reasonable level of accuracy (comparable to rVV10) in wide class of systems, moreover the additional cost with respect to a standard GGA calculation is only 30 %.

Although it improves the description of vdW interactions over conventional semi-local DFT, a systematic error of this kind of approach is the consistently overestimate of inter-fragment distances. This happens because, in its original version, vdW-DF was combined with revPBE [42] exchange functional that is too repulsive at small separations [43].

By trying to overcome this limitation, subsequent investigations led to the conclusion that the following properties are required [44] for a suitable exchange functional to equip vdW-DF with.

- If we define an enhancement factor for the exchange functional

$$F_X(s(\vec{r})) = 1 + \mu s(\vec{r})^2 \tag{2.23}$$

  where s has been introduced in (2.13) and $\mu \approx 0.1$, then the first criterion that a suitable exchange functional for vdW-DF has to satisfy is that, in the slow-varying density limit

($\nabla n(\vec{r}) \to 0$), its enhancement factor has to have the same dependence as the one in (2.23). This property plays an important role in predicting equilibrium geometries for solids and surfaces [45].

- At large gradient limit ($\nabla n(\vec{r}) \to \infty$), it is proposed [45] that the enhancement factor should have a $s(\vec{r})^{2/5}$ dependence, so that it can avoid the spurious binding from exchange only.

In this spirit, a recent promising development presented in the next subsection was introduced by Hamada.

vdW-DFq Method

Hamada proposed another exchange functional [46] (vdW-DFq), improving the description of attractive vdW interactions near the equilibrium with respect the original vdW-DF.
The vdW-DFq enhancement factor reads:

$$F_X(s(\vec{r})) = 1 + f_q \mu_0 s(\vec{r})^2$$
$$f_q(s(\vec{r})) = \frac{1}{(1 + \mu_0 s(\vec{r})/q)^{4/5}}$$

When $s \to 0$, then $f_q \to 1$ and the first condition mentioned above is fulfilled.
The angular coefficient of the asymptote of the enhancement factor represents an important quantity for binding separations[47] and reads:

$$\frac{d\,F_X(s(\vec{r}))}{d\,s(\vec{r})} = 2\mu_0 f_q(s(\vec{r}))s(\vec{r}) - \frac{1.8\mu_0^2 f_q(s(\vec{r}))^{9/4}}{q\,s^3}$$

The value of the parameter q is established in such a way that the asymptote of $F_X(s(\vec{r}))$ for $s \to \infty$ is such that the second condition mentioned above is fulfilled. We can notice that such a method based on this parametric optimization can really tune the quantitative nature of the exchange functional, permitting to explore a wide range of values for the enhancement factor and its derivative; even if it is clear that an universal and accurate function for the enhancement factor might be very hard to find. However, it can be useful to tune the enhancement factor for particular kinds of materials that have similar electronic charge density reduced gradients $s(\vec{r})$. We will return on this point in the conclusions of this work.
In a very recent study [45], different kinds of materials belonging to the class of semi-hard materials have been tested to provide an opportune tuning of the q parameter in order to optimize the mass density.
In this work a further modification of the q parameter was proposed, suggesting that the mass density is optimized for $q_2 = 1.05$. In particular, several DFT calculation on energetic materials are performed, for which the mass density is a fundamental parameter, since it is strongly related to the energy density and consequently to the detonation performance [45]. Interestingly, part of the study was focused instead on MoS_2 that belongs to the class of transition metal dichalcogenides, exactly as TiS_2.

2.3 Computational Details

Our calculations have been performed using the Quantum ESPRESSO (QE) package [21]. Quantum ESPRESSO is a suite for ab initio condensed matter and quantum chemistry methods of electronic-structure calculation and materials modeling, distributed for free under the GNU General Public License. It is based on Density Functional Theory, plane wave basis sets, and pseudopotentials (both norm-conserving and ultrasoft). ESPRESSO is an acronym for opEn-Source Package for Research in Electronic Structure, Simulation, and Optimization.
The purpose of this brief section is to discuss the main principles this DFT package in based on.

2.3.1 Plane wave basis

First of all, it is useful to introduce the Bloch theorem, that is a well-known result in condensed matter physics. Let us consider a crystal lattice in which there is a periodic potential of the form:

$$U(\vec{r}) = U(\vec{r} + \vec{R})$$

$$\vec{R} = \sum_{i=1}^{3} c_i \vec{a}_i$$

where $\vec{R}$ is a crystal vector in the real space and $\vec{a}_i$ define the three directions along which the crystal is built.
The motion of an electron in such a periodic potential, is governed by the quantum Hamiltionian

$$H = -\frac{\nabla^2}{2} + U(\vec{r})$$

The Bloch theorem states that the eigenstates of this electron are of the form

$$\psi_{n\vec{k}}(\vec{r}) = e^{i\vec{k}\cdot\vec{r}} u_{n\vec{k}}(\vec{r}) \tag{2.24}$$

where $u_{n\vec{k}}(\vec{r})$ is a function with the same periodicity of the lattice (i.e. $u_{n\vec{k}}(\vec{r}) = u_{n\vec{k}}(\vec{r} + \vec{R})$ for all $\vec{R}$ in the Bravais lattice), and n is the so called "band index" accounting that for a given wavevector $\vec{k}$, there are many independent eigenstates.
According to this result, the KS orbitals ϕ appearing in (2.2) can be computed summing on all the wavevector the Bloch waves of the form (2.24)

$$\phi_n(\vec{r}) = \sum_{\vec{k}} \psi_{n\vec{k}}(\vec{r}) = \sum_{\vec{k}} e^{i\vec{k}\cdot\vec{r}} u_{n\vec{k}}(\vec{r}) \tag{2.25}$$

However, since this sum is practically infinte, QE introduces a kinetic energy cutoff (KEC) that in practice determines the number of Bloch Waves used to determine the KS orbitals.
From a computational point of view the introduction of a suitable KEC is obviously convenient, although it represents an approximation. More specifically, if the KEC is not very high, the Bloch wave basis set is not enable to reproduce the oscillations of the wavefunctions associated to the core-electrons but only to describe well the ones of the valence electrons. This problem can be addressed by adopting the pseudopotential theory described in the following section.

One should also point out that, using plane waves as a basis set for the electronic structure calculations has several important advantages. For instance, by adopting this scheme, a uniform space sampling is guaranteed, leading to the same accuracy in all the spatial points. Further, the convergence of the physical quantities can be governed by a single parameter, that is the KEC.

2.3.2 Pseudopotentials

It is very difficult to deal with highly localized states such as core electrons due to strong ionic potential in this region. In the majority of software of modern electronic structure calculations, including QE, the Coulombian interaction between electrons and nuclei is pseudized and replaced by smooth potentials, as showed in figure 2.2, causing slowly varying densities in the core of the atoms. The pseudopotential approximation was first introduced by Hans Hellmann in 1934 and, in this approach, valence states should be orthogonal to the core states and therefore they can be described using a limited number of plane waves, making the above mentioned approximation of using a KEC suitable. In principle, core electrons are treated as frozen electrons since they give no contribution to the formation of chemical bonds. Therefore, the only contribution comes from valence states. More specifically, in the context of practical DFT calculations, one can introduce a core-cutoff radius r_c as a threshold to separate the core and valence contributions.

Several important schemes are devised for pseudopotential approximation, among which we can cite the Norm-Conserving-PseudoPotential (NCPP) [48] together with Ultra Soft PseudoPotential (USPP) [49], that represent two of the most popular approaches within DFT calculations.

NCPP is constructed on the basis of the following two constrains:

- Within the cut-off core radius r_c, the norm of each pseudo-wavefunction has to be identical to the one of the corresponding all-electron wavefunction.

- Above r_c, is required that each pseudo-wavefunction has to be identical to the real all-electron wavefunction.

The presence of these two constrains, practically means to adopt an high KEC, leading to considerable high computational costs. For this reason, one usually refers to NCPP as an "hard" pseudopotentials, indicating its reliability to describe the wide oscillations of strongly bounded electrons.

USPP relaxes the constrain on the norm conservation to reduce the necessary plane wave basis set size. This is done choosing a larger value of r_c, making the pseudopotential more "*soft*" with respect to NCPP. Thus, within this approach, the computational cost is reduced, but at the prize to introduce (see ref. [50]) a more complicated computation scheme for the charge density.

A more recent approach is the Projector Augmented Wave (PAW) [51]. This scheme, derived from linear-augmented-plane-wave methods, allows for DFT calculations to be performed with great computational efficiency, because transforms the rapidly oscillating valence wavefunctions into more computationally convenient smooth wavefunctions.

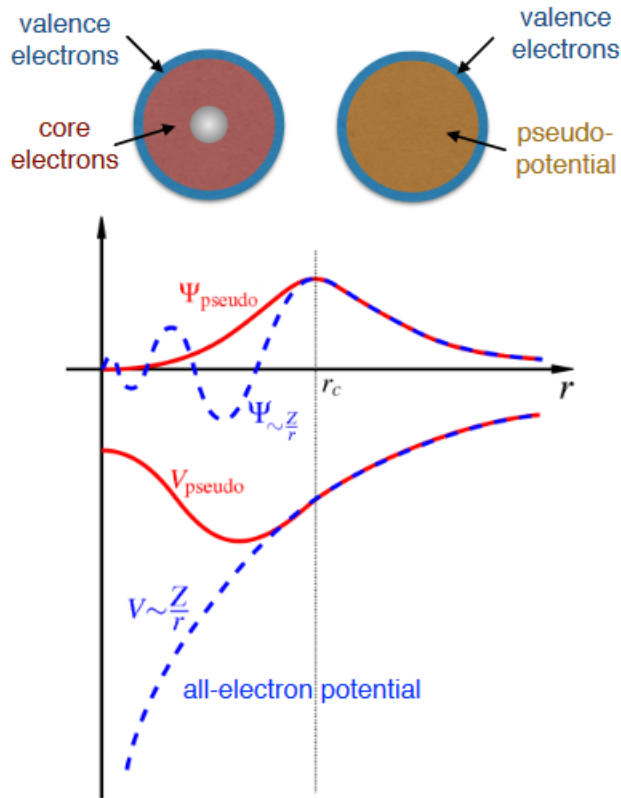In this thesis, PAW and USPP schemes are adopted.

Figure 2.2: Schematic approximation adopted in the Pseudopotential framework.

2.3.3   The Self-Consistent Scheme

The resolution of KS equations is carried out within a self-consisted scheme (SCS) (figure 2.3), and, in the spirit of the Pseudopotential approximation, this will be applied only to the valence electrons, taking the core electron contribution frozen into the external potential (term $V(\vec{r})$ in (2.4)).

Such an approach is required since in the KS equations (2.2) both V_{XC} and the Hartree contribution, are functionals of the electronic density $n(\vec{r})$. The same density depends on KS eigenfunctions ϕ_i through (2.3) but, in turn, ϕ_i can be determined with the knowledge of the total effective potential V_{eff} in (2.4).

Once the nuclear potential is determined thorugh the pseudopotential approximation, QE creates a suitable configuration of the electronic density $n_0(\vec{r})$, so that it is possible to completely determine the effective potential in (2.4).

The solution of the KS equation is obtained computing the matrix elements of KS Hamiltonian:

$$\langle \phi_n | \left(-\frac{\nabla^2}{2m} + V_{eff} \right) | \phi_{n'} \rangle = \epsilon \langle \phi_n | \phi_{n'} \rangle$$

A diagonalization procedure yields the new eigenfunctions $\phi_n^{(D)}$ from which it is possible to compute a revised profile for the electron density $n_1(\vec{r})$.

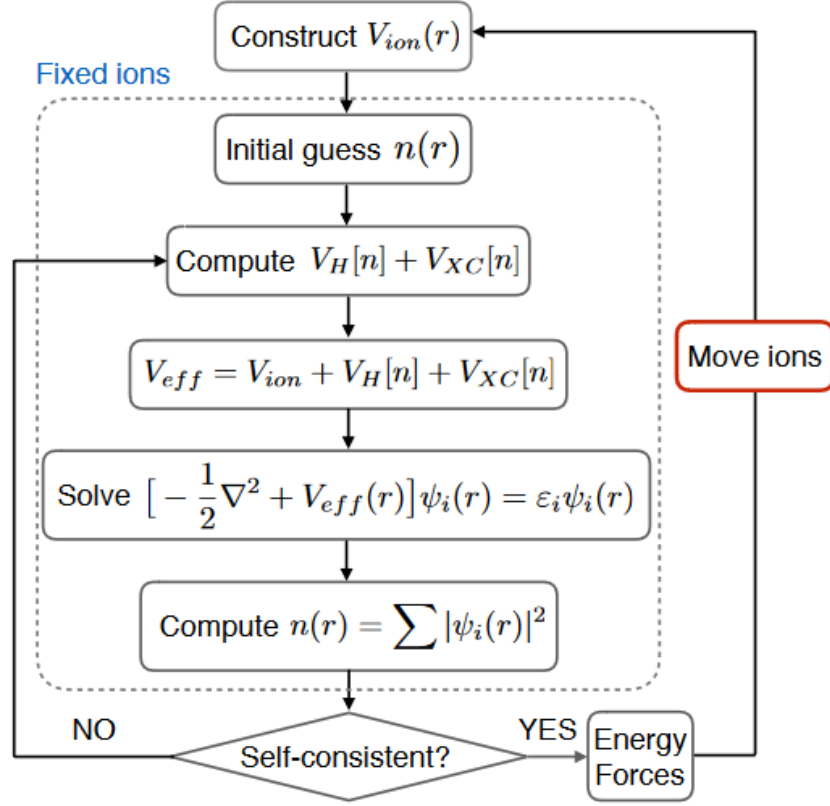More specifically, this calculation is performed with a suitable k-points grid (GR) within the first

Figure 2.3: Self-Consistent Scheme.

Brillouin zone, whose thickness is decided by the user:

$$n_1(\vec{r}) = \sum_n \left|\phi_n^{(D)}(\vec{r})\right|^2 = \sum_n \sum_{\vec{k}} \left|\psi_{n\vec{k}}^{(D)}(\vec{r})\right|^2 \rightarrow \frac{1}{\Omega_{BZ}} \sum_n \int_{GR} d\vec{k} \left|\psi_{n\vec{k}}^{(D)}(\vec{r})\right|^2$$

Where first we have made use of (2.25), considering the Bloch waves ψ and then we have transformed the summation over $\vec{k}$ into an integral in momentum space normalized with respect to Ω_{BZ}, the volume of the first Brillouin zone.

Obviously, a thicker mesh of k-points will give more precise results, but it will be more computationally expensive.

In general, the new density profile is computed as a weighted average of the old density n and the new density n_1 and the weight can be decided by the user.

Once the profile of $n_1(\vec{r})$ is evaluated, the total energy of the system $E_1[n_1(\vec{r})]$ can be recomputed. If the error ΔE_1 associated to E_1 is smaller than a convergence thresold C, then the SCS ends. Otherwise, the scheme is repeated, until the convergence is reached.

Chapter 3

Results

In this section, the results obtained in this thesis work, applying the DFT ab-initio methods described in the previous section, are presented.

Initially, we made a structural and energetic analysis on bulk Ti and S crystals separately, thus testing PAW and USPP pseudopotentials. The purpose of such a work scheme, is to determine the pseudopotential type that allow to get the better theoretical prediction, in order to subsequently apply to the study of TiS_2.

Then, taking advantage of the above described procedure, structural, energetic and electronic properties of TiS_2 will be computed and discussed, paying particular attention to the behavior of the electronic charge density predicted in *interlayer* and intralayer fragments.

All the graphics presented in this section are made with the software Gnuplot [52] and XCRYSden [53].

3.1   Titanium

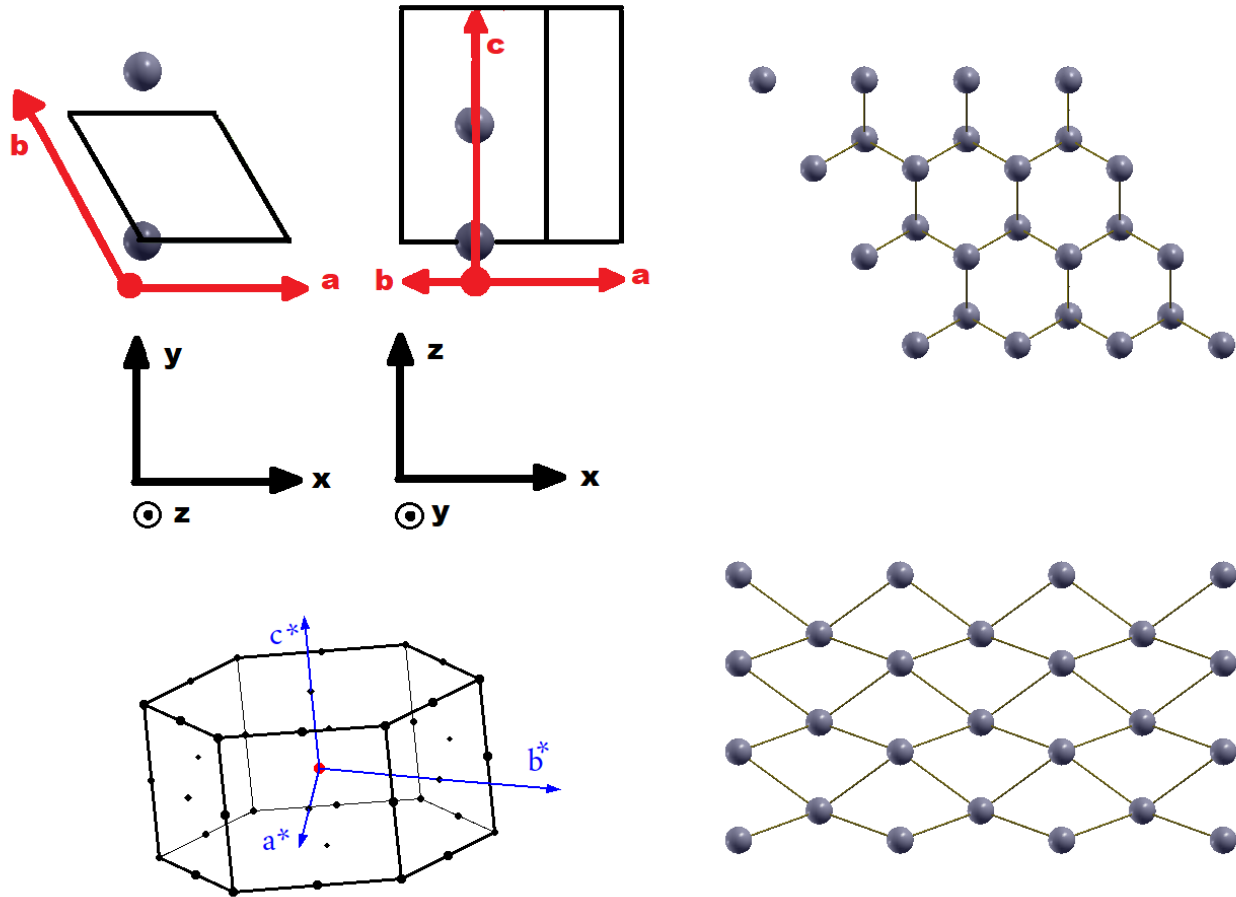Titanium is a transition metal with atomic number 22, whose electronic configuration is $[Ar]3d^24s^2$.

Figure 3.1: HCP α-phase of Titanium.

The crystal structure of titanium at ambient temperature and pressure is α hexagonal close-packed (HCP) (slip with higher energy it is possible on the pyramidal, prismatic and basal planes in the close-packed directions).
This structure can be characterized by two reticular parameters: a, that is the hexagonal side on the plane and c, that is referred to the development of the structure along the vertical axis.
This crystal has a two-atom basis that is repeated, according to an hexagonal symmetry, considering the basis vectors:

$$\vec{a} = a\,(1\,,0\,,0)^T$$
$$\vec{b} = a(-1/2\,,\sqrt{3}/2\,,0)^T$$
$$\vec{c} = a(0\,,0\,,c/a)^T$$

This leads to an hexagonal Brillouin zone, whose primitive vectors are

$$\vec{a^*} = 2\pi/a \, (1\,,-1/\sqrt{3}\,,0)^T$$
$$\vec{b^*} = 2\pi/a \, (0\,,2/\sqrt{3}\,,0)^T$$
$$\vec{c^*} = 2\pi/c \, (0\,,0\,,1)^T$$

At about 1163 K, Ti undergoes an allotropic transformation to a body-centered cubic β-phase which remains stable up to the melting temperature.

ω is a metastable phase, which can be reached both from α- and β- phases and its formation generally leads to a deterioration in the mechanical properties of the material. Exactly as the α-phase, also the ω-phase is characterized by HCP structure, but with a smaller c/a ratio.

For our purposes it is sufficient to evaluate the reticular constants a and the c/a ratio of a pure α-phase, and the cohesion energy of the minimum-energy configuration.

3.1.1 Convergence parameters optimization

The first operation that has to be carried on, is the optimization of the following parameters:

- E_{cut}.

- nk.

- E_{smear}.

The first two parameters are respectively the KEC and the number of points of the k-grid in the reciprocal space, discussed in the last section of the previous chapter. In particular, since we will always employ cubic grids, we refer to nk as the number of point considered in the cubic side of the mesh, which contains n$k \times$ n$k \times$ nk points. When this is not the case it will be specified.

The last cited parameter is particularly important for metallic systems. In order to understand its meaning, just think that, according to the Fermi-Dirac distribution at absolute zero, the electrons of a generic system will always occupy the lowest eigenstates up to a given energy. If there are several degenerate (or close to degenerate) eigenstates at the Fermi level, it is possible to get convergence problems, since very small perturbations may change the electron occupation.

One method of reducing these effects is to "smear the electrons", that means to allow fractional occupancies. There are a few different approaches to do so, for instance, assigning a finite temperature to the electron Fermi–Dirac distribution will smoothly modify the step-like nature, fixing the convergence problem. Another way is to assign a cumulative Gaussian distribution to the electrons, that is the method that we have used in this work.

To optimize the three parameters, first of all we have build up the unit cell of Ti α-phase as it is shown in figure (3.1) and then, fixing the values for the lattice constants a and for the c/a ratio to a=2.951 Å and c/a=1.587, according to the experimental values cited in literature (see ref. [54]), we have performed several self-consistent calculations, looking for the convergence of the total energy of the system E_{tot}. This is done by employing both PAW and USPP pseudopotentials.

It is important to underline that the convergence of the total energy with respect to nk, depends also on the electron smearing, and so an analysis of the trend of $E_{tot}(E_{smear})$ with respect to different values of nk is required. Furthermore, in order to not excessively perturb the computed values of the total energy, is convenient to take the smearing factor as little as possible.

The optimized values of these three parameters are chosen making a compromise between precision and computational cost at the same time, searching a configuration of these three parameters allowing to reasonable results at an acceptable computational cost. The result of this analysis are presented in figure (3.2) and figure (3.3) and summarized in table (3.1).
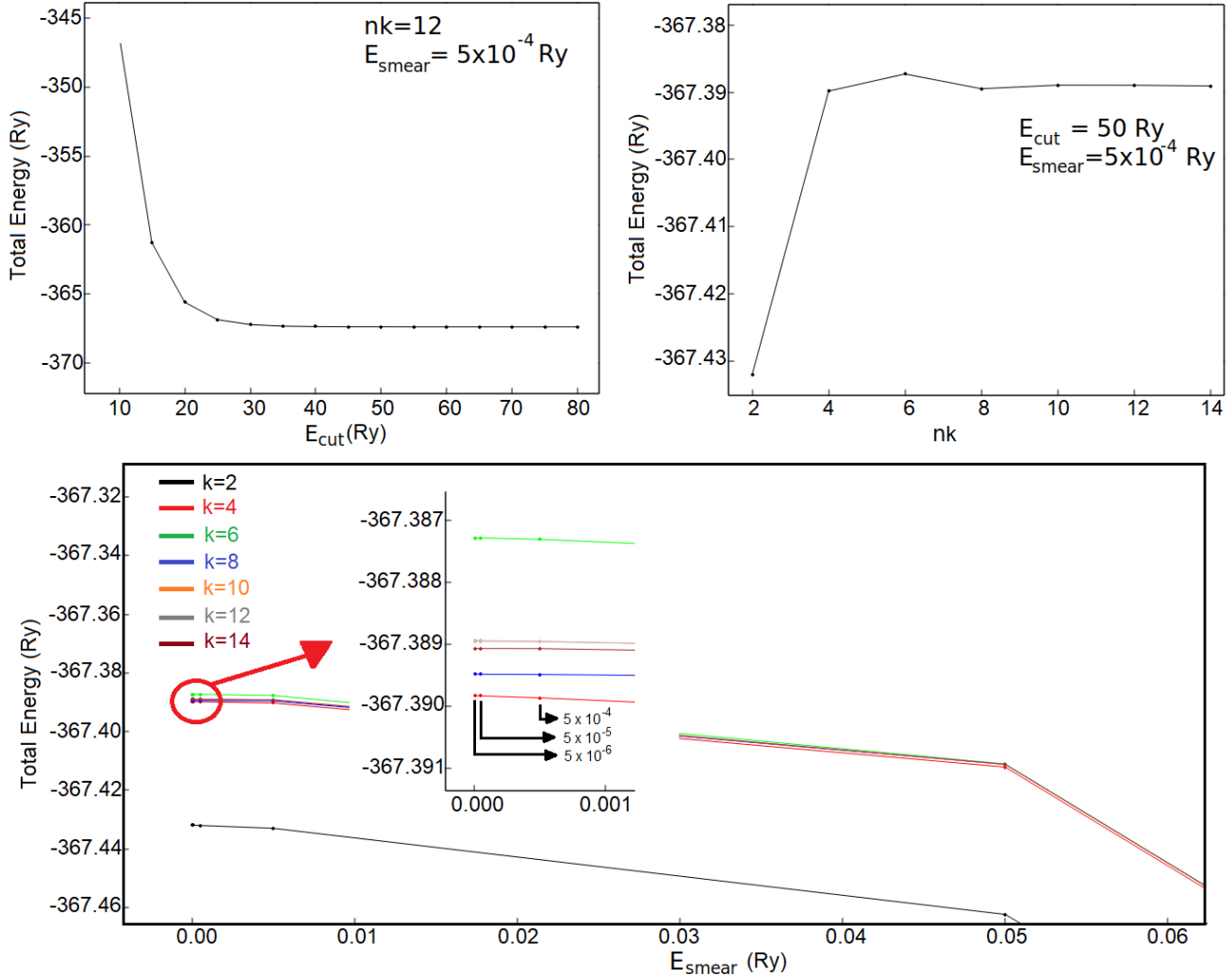

Figure 3.2: Analysis of the three convergence parameters using PAW pseudopotential for titanium. In the bottom figure there is an analysis of the smearing factor, as a function of the total energy, for different values of k.
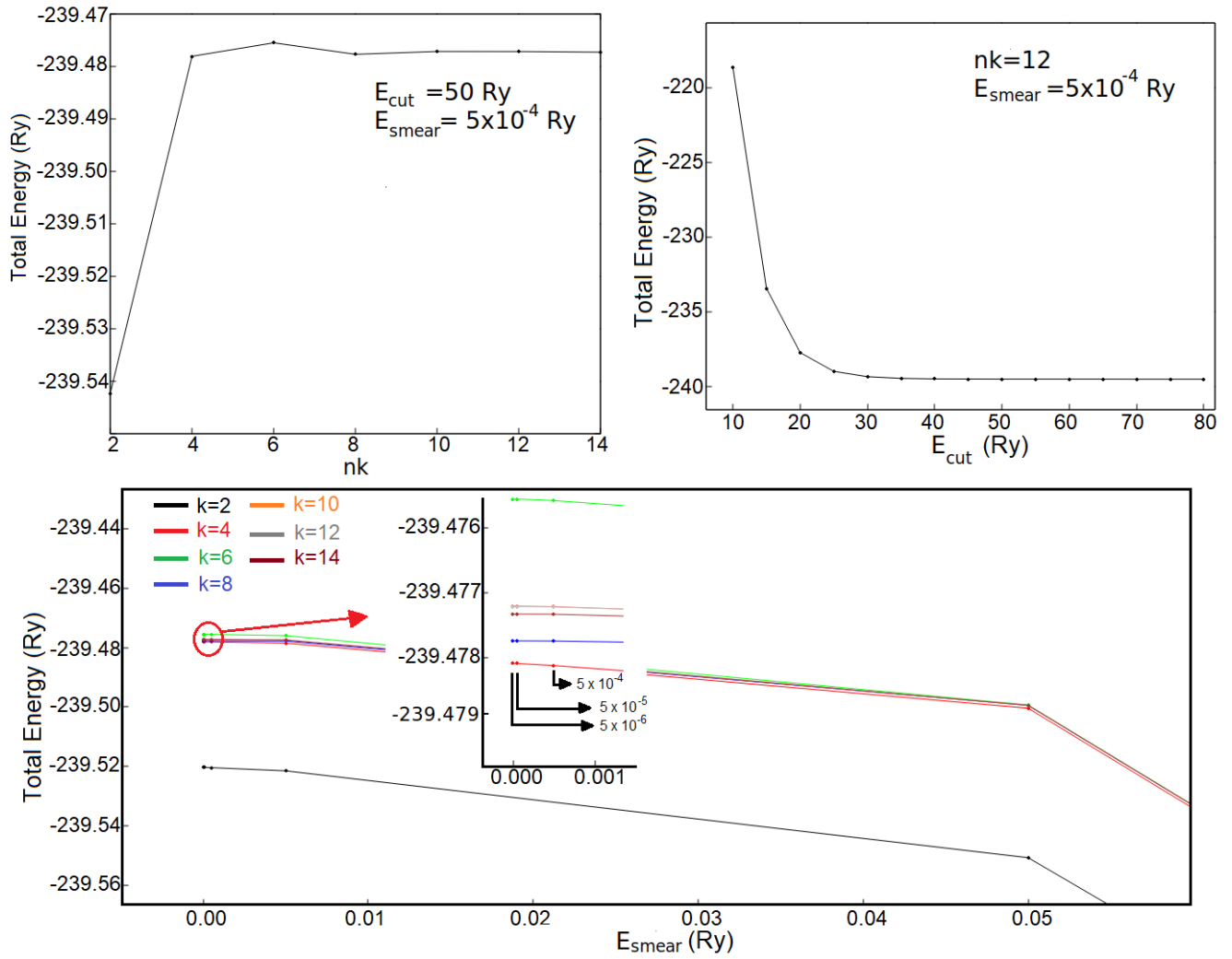
Figure 3.3: Analysis of the three convergence parameters using USPP pseudopotential for titanium. In the bottom figure there is an analysis of the smearing factor, as a function of the total energy, for different values of k.

	PAW	USPP
E_{cut} (Ry)	50	50
nk	12	12
E_{smear} (Ry)	5×10^{-5}	5×10^{-5}

Table 3.1:   Summary of the values of the three convergence parameters optimized, for both PAW and USPP pseudopotentials.

3.1.2 Structural and energetic analysis

Once E_{cut}, nk and E_{smear} are optimized both for PAW and USPP pseudopotential scheme, a structural analysis for the Ti α-phase can be carried out, again applying the two kinds of pseudopotentials.

Now, the purpose is to predict the lowest-energy configuration for this crystal and then to estimate its cohesion energy. The pseudopotential giving the best agreement with literature data will be used in the treatment of TiS_2. In order to determine the lowest-energy configuration we have performed several self-consistent calculations with different values of the reticular constants, looking for the ones that minimizes the total energy of the crystal.

In particular, this analysis is carried on within a GGA framework, employing a pure **PBE** functional. The procedure consists in the following steps:

- Relaxation of the atomic positions, until the total force acting on the atoms of the crystal is smaller than a threshold fixed to 10^{-5} Ry/a.u..

- Optimization of a, fixing c/a=1.587 (see ref [54]): $a \rightarrow a_{min}$.

- Optimization of c/a, fixing $a = a_{min}$: $c/a \rightarrow (c/a)_{min}$.

- Computation of the cohesion energy of the system employing a_{min} and $(c/a)_{min}$.
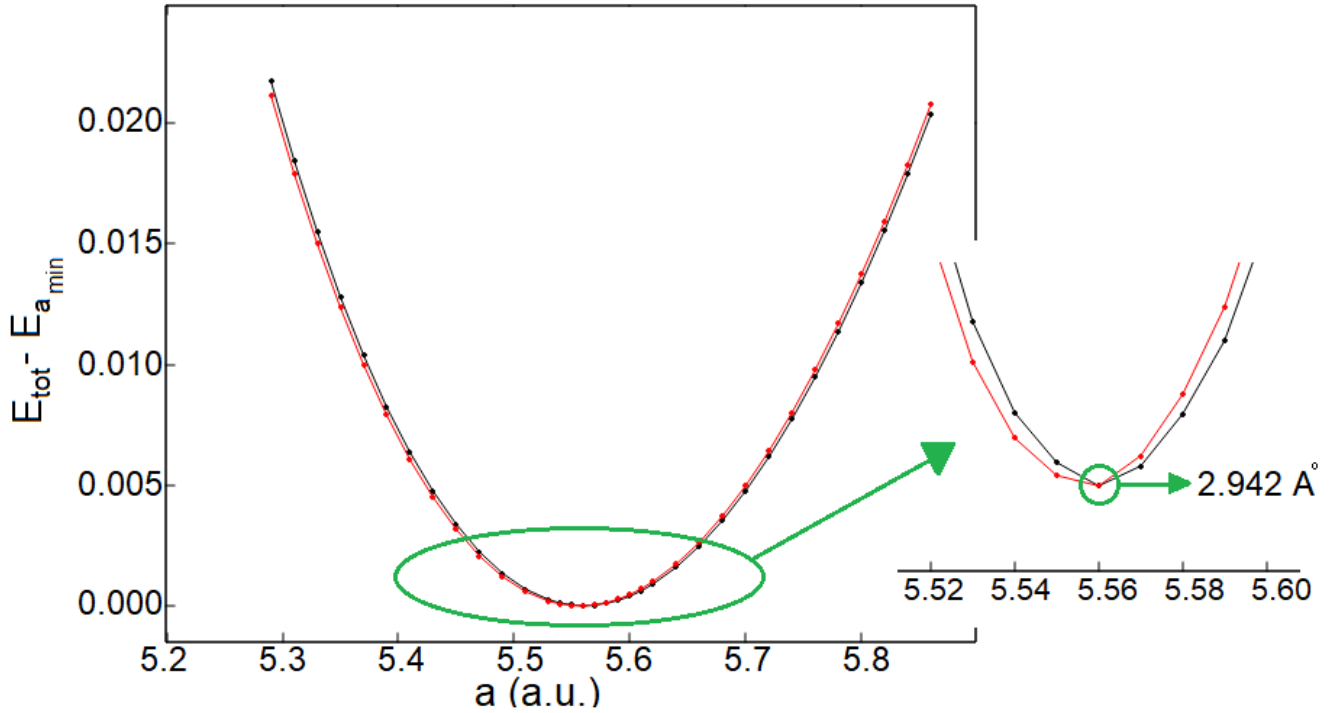

Figure 3.4: $E_{tot} - E_{a_{min}}$ as a function of different values of the hexagonal reticular constant a, for both the pseudopotential schemes employed. In red the curve computed within PAW, in blue the one associated to USPP.
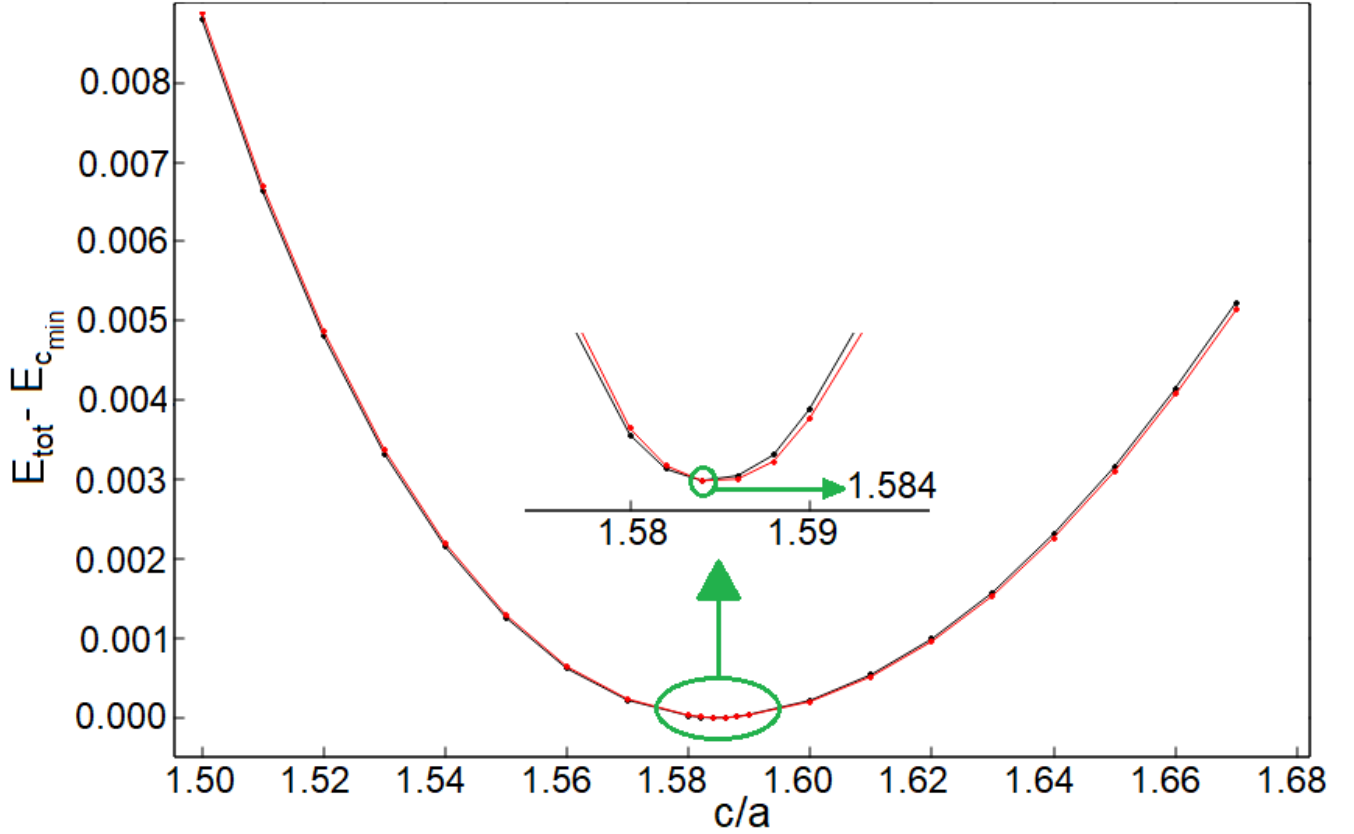
Figure 3.5: $E_{tot} - E_{c_{min}}$ as a function of different values of the c/a ratio, for both the pseudopotential schemes employed. In red the curve computed within PAW, in blue the one associated to USPP.

The trends of the energy as a function of the lattice constants obtained after the relaxation process, are presented in figure (3.4) and (3.5) and all the results, including the computation of the cohesion energy, are summarized and compared with literature data in table (3.2).

	PAW	USPP	References
a_{min} (Å)	2.942	2.942	2.951 [54]
c_{min}/a_{min}	1.584	1.584	1.587 [54]
E(Ti-α)-2E(Ti$_{atom}$) (eV)	-10.251	-10.180	-9.700 [55]
(E(Ti-α)-2E(Ti$_{atom}$))$_{ref}$ (eV)	-10.250	-10.179	

Table 3.2: Structural parameters and cohesive energy computed for the Ti-α phase, both for PAW and USPP pseudopotentials. Here, the cohesive energy is computed as the difference between the Energy of the 2-atom basis, and 2 times the energy of a single Ti atom. In the third row, the former term of such a difference is assumed to be the energy of the atom basis within the most energetically convenient configuration predicted and the latter is the energy of a Ti atom inside a cubic supercell with a side of 10 Å. In the last row, we have used the experimental parameters of ref. [54] for the computation of E(Ti-α).

The agreement obtained in the prediction of the reticular constants is extremely good for both PAW and USPP pseudopotentials. In the case of a, we have an agreement within 0.3%, instead, for the c/a ratio, the error is smaller than 0.2 %.

It is important to point out that, in order to get a reliable estimate of the Ti cohesion energy, a proper description of spin effects is mandatory. In fact, although the ground-state configuration of the bulk α-Ti structure has zero spin, the lowest energy configuration (d^2s^2) of the isolated Ti atom has a non vanishing spin.

To be more precise, DFT calculations at the GGA level predict (see ref. [56]), that the actual Ti ground state is d^3s^1, since the 3d and 4s energy levels are almost degenerate.

Proceeding in this way, satisfactory results are achieved. Both PAW and USPP predict a slightly more bounded state with respect to the one of ref. [55]. In particular the USPP result shows an error less than $\approx 5\%$ and the PAW result is found to be ≈ 5.7 % below the experimental value of [55].

Since the USPP result for the cohesion energy result slightly more in agreement with the reference data, we decide to employ USPP pseudopotential for Titanium in the further treatment of TiS_2.

3.2 Sulfur

Sulfur is a versatile, and non-metallic chemical element with atomic number 16 and electronic configuration [Ne] $3s^2\ 3p^4$. Under normal conditions, Sulfur atoms form cyclic octatomic molecules with a chemical formula S_8. Sulfur is a bright yellow crystalline solid at room temperature.

It can crystallize in around thirty different phases depending on pressure and temperature, a number that makes it the chemical element with the highest number of allotropic states in the periodic table. At ambient pressure it forms structures with a very small packing factor. Twenty of those are composed of molecular rings with six to twenty sulfur atoms each. There also exist polymeric structures formed by molecular chains. As pressure increases the structures get more closely packed, and in the megabar regime Sulfur becomes a metal with a superconducting temperature of 17 K. At ambient conditions the most stable phase of sulfur is α-S, in which S_8 ring molecules crystallize in the orthorhombic space group, as it is shown in figure (3.6).
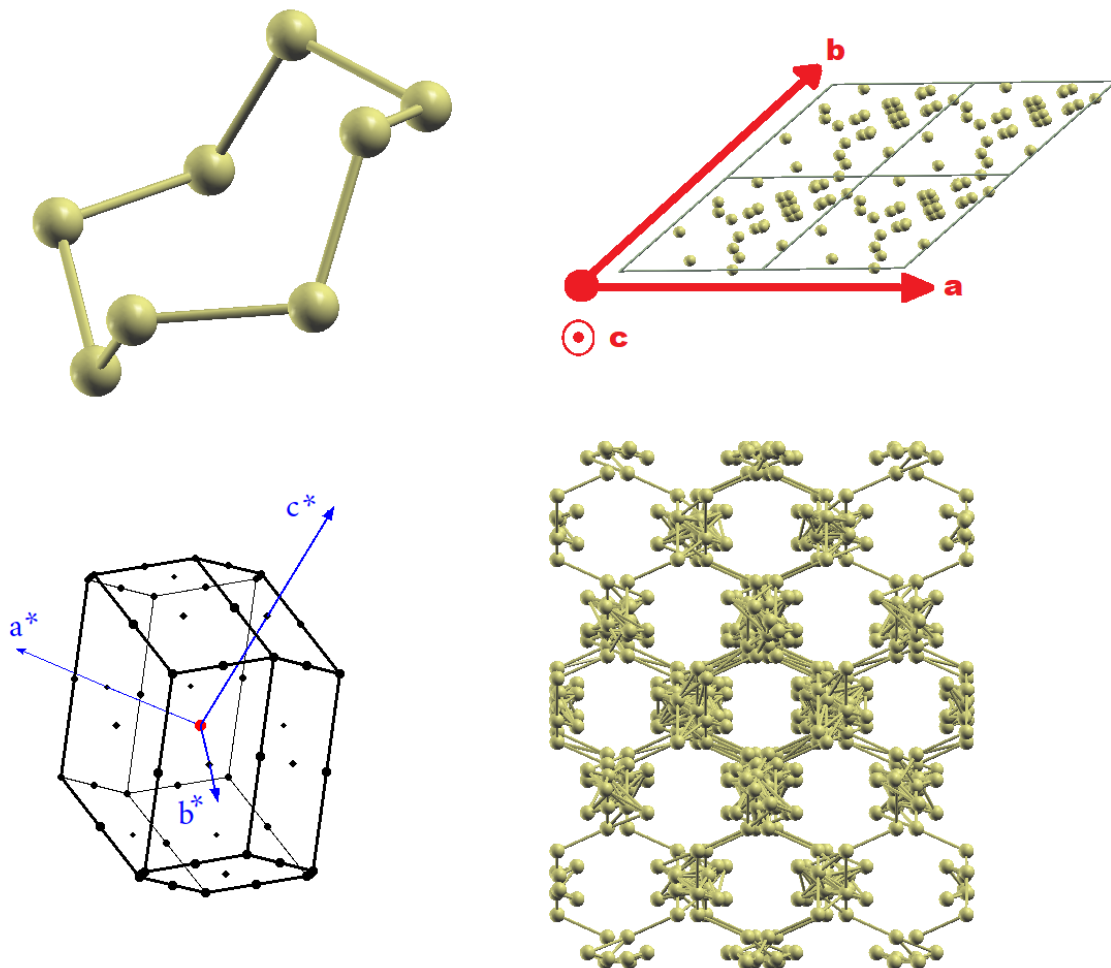

Figure 3.6: S_8 molecule, and bulk structure of the α orthorhombic Sulfur with associated Brillouin zone.

Given the complexity of the S phases, we have tested the performances of PAW and USPP pseudopotentials by studying the geometrical twisting of a S_8 molecule both as an isolated fragment and as a bulk α-S structure.

The data of the unit cell and of the atomic positions of α-S have been taken from ref. [57].

Here, we have not repeated the parameters optimization and we have adopted the same values chosen for Ti. In fact the $E_{cut}^{(Ti)}$ value turns out to be appropriated to describe accurately TiS_2, which is the system we are mostly interested in.

Moreover, since Ti is a pure metal, differently from S, we expect that both $nk^{(Ti)}$ and $E_{smear}^{(Ti)}$ are also appropriated for TiS_2, since these parameters are more delicate to be optimized for metals.

3.2.1 Investigation of the twisting of a S_8 molecule

Since it is well-known that the vdW interactions strongly contribute to the deformation of the S_8 molecule [58], we have employed the rVV10 non-local exchange-correlation functional investigate the S_8 geometry.

In the case of an isolated S_8 ring, the procedure consists in two steps:

- Relaxation of the atomic positions until the total force acting on each S atom is smaller than a threshold fixed to 10^{-5} Ry/a.u..

- Evaluation of the S-S bond lengths and of the bond angles in the relaxed configuration determined above.

To study the geometrical properties of a S_8 ring within an α-S bulk structure, the procedure is similar, but, because of the very complicated nature of the the α-S bulk, the relaxation procedure is more complex.

In fact, extended simulations showed that the system is characterized by several local minima, almost isoenergetic and exhibiting not too different structural basic parameters. Therefore, we have investigate the twisting of the S_8 molecule by choosing one of these local-minimum configuration, without claiming to find the absolute minimum structure.

BULK		MOLECULE	
USPP			
Bond Lenght(Å)	Angle (°)	Bond Lenght (Å)	Angle (°)
2.058	109.191	2.069	109.327
2.053	109.467	2.070	109.302
2.059	108.410	2.070	109.322
2.063	109.271	2.070	109.357
2.058	108.085	2.069	109.317
2.054	107.483	2.070	109.319
2.053	109.001	2.070	109.317
2.054	108.724	2.070	109.330
Means & [Experimental reference][59] & (Theoretical reference)[58]			
2.056 [2.055]	109.304 [108.200]	2.070 (2.070)	109.323 (109.3)
PAW			
Bond Lenght (Å)	Angle (°)	Bond Lenght (Å)	Angle (°)
2.059	109.359	2.069	109.301
2.069	109.071	2.069	109.216
2.063	109.324	2.071	109.303
2.068	109.283	2.071	109.278
2.063	109.351	2.069	109.304
2.068	109.173	2.069	109.210
2.064	109.201	2.071	109.310
2.065	109.193	2.071	109.279
Means & [Experimental references][59] & (Theoretical references)[58]			
2.065 [2.055]	109.344 [108.200]	2.069 (2.070)	109.275 (109.3)

Table 3.3: Summary of the bond lengths (nearest neighbours S-S distances) and relative bond angles for the S_8 molecule, both as isolated and within a bulk α-S, employing PAW and USPP pseudopotentials.

The detailed analysis shows an extremely good agreement of the bond lengths and angles for both PAW and USPP with the reference values. Although the results achieved with PAW are already very good, the ones of USPP are even slightly better.

In particular, in the case of an isolated S_8 ring, using USPP, we obtain a perfect agreement of the mean bond lenght with respect to ref.[58]. For the bond angles, we find an error of only 0.02% with respect to another theoretical calculation performed within a vdW-corrected DFT scheme (ref. [58]).

In the case of S_8 within the α-S structure, we obtain again good results: for the mean bond lenght we have an error of 0.5 % with respect to [59] that is an experimental reference, instead, in the case of the mean bond angle, the result is slightly worse but again in appreciable agreement, showing an error of 1%.

Since the results for the geometrical twisting of the S_8 molecule applying USPP are in a slightly better agreement with literature data, with respect to the one obtained with PAW, we have decided to apply USPP also for Sulfur in the treatment of TiS_2 presented in the next section.

3.3 Titanium Disulfide

In the following section the results of the ab initio calculations relative to TiS_2 are presented.
First of all, we have focused on the structural properties, making an analysis similar to the one carried out in the previous case of α-Ti. In particular, since TiS_2 has an hexagonal symmetry, we have computed the two lattice parameters a and c, and then, in the most energetically convenient configuration predicted, we have made an estimation of the cohesion energy (CE) and of the *interlayer* binding energy (ILBE).
The next point we have analyzed is the computation of the charge density, both in intralayer and *interlayer* regions. This is done to characterize the chemical bonds, focusing on the specific effect of the vdW interactions. In order to validate the results obtained in our approaches, all the data presented will be compared with other literature data, both experimental and theoretical.
TiS_2 is a transition metal dichalcogenide (TMD), whose basis is composed by two atom of S and one of Ti periodically repeated, according to an hexagonal symmetry, along the directions

$$\vec{a} = a\,(1\,,0\,,0)^T$$
$$\vec{b} = a(-1/2\,,\sqrt{3}/2\,,0)^T$$
$$\vec{c} = a(0\,,0\,,c/a)^T$$

This leads to an hexagonal Brillouin zone, with the same shape of the one shown in figure (3.1), whose primitive vectors are

$$\vec{a^*} = 2\pi/a\,(1\,,-1/\sqrt{3}\,,0)^T$$
$$\vec{b^*} = 2\pi/a\,(0\,,2/\sqrt{3}\,,0)^T$$
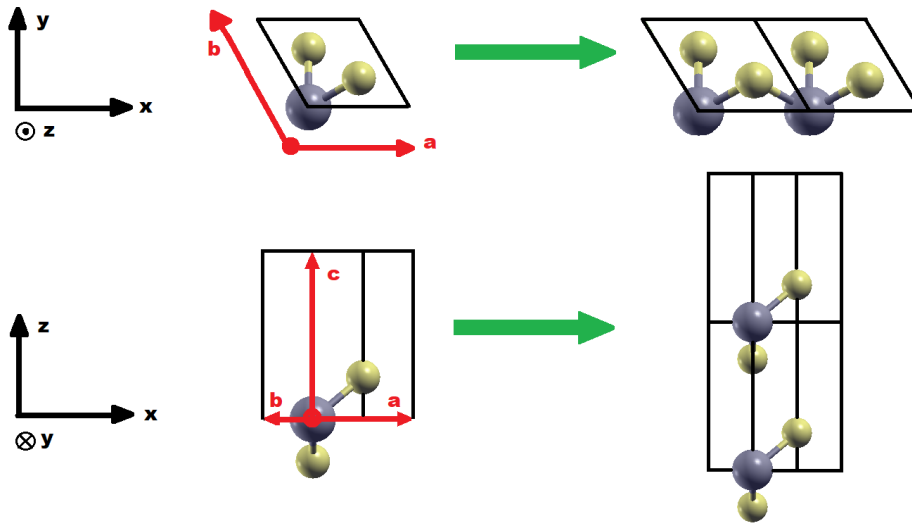$$\vec{c^*} = 2\pi/c\,(0\,,0\,,1)^T$$

Figure 3.7: 3-atom basis of TiS_2 and structural development of the solid on the x-y plane and along the longitudinal direction.
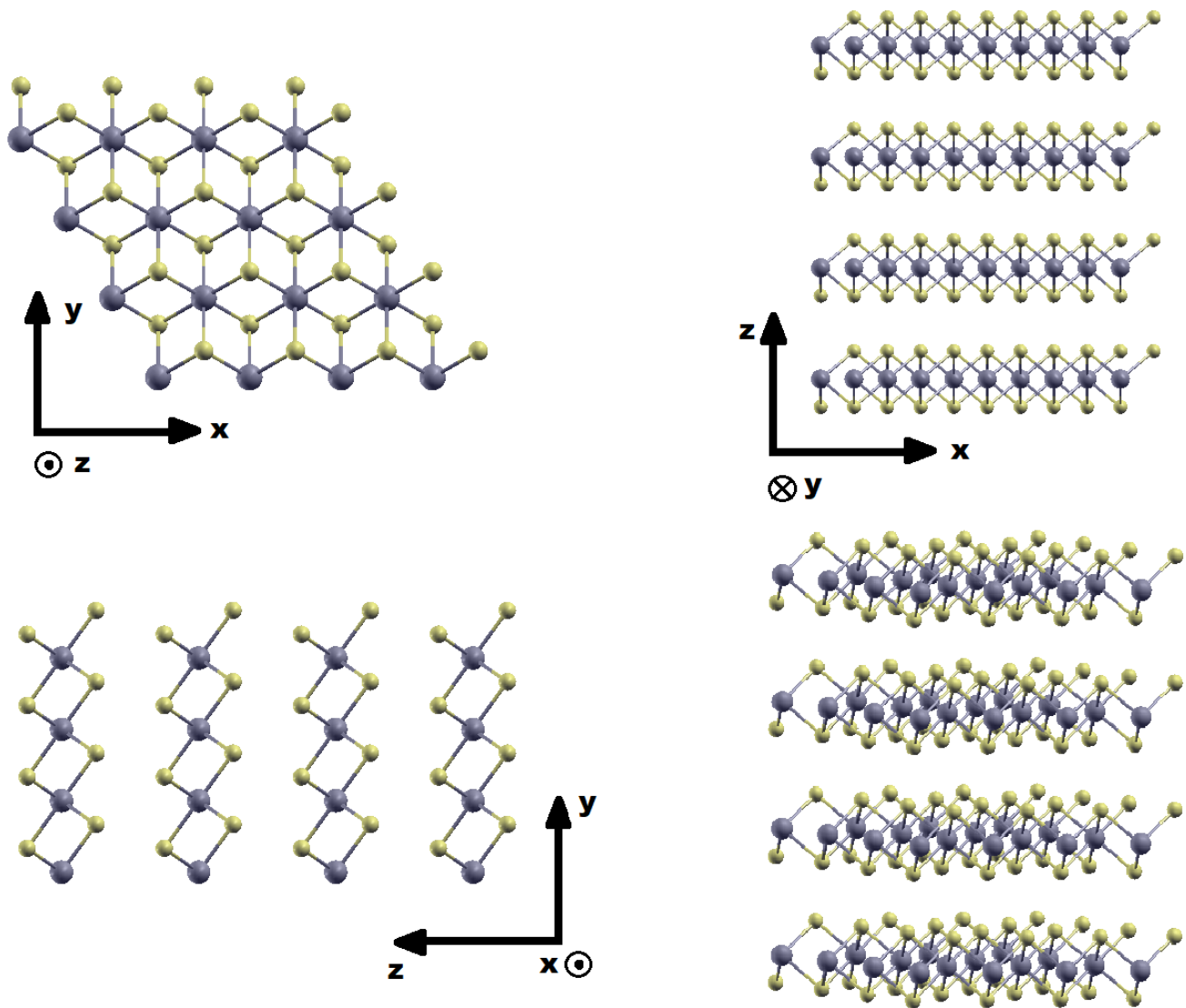
Figure 3.8: Bulk of 4×4×4 translation-symmetric units by adopting different perspectives.

3.3.1 Structural and energetic analysis of TiS$_2$

We have applied six different functionals, including vdW interactions at different levels, in order to evaluate the lowest energy configuration of TiS$_2$ at T=0.

The relaxation process of the atoms belonging to the 3-atom basis is performed first considering the parameters a =3.398 Å and c/a=1.667, according to the literature data [20]. Once the atomic positions have been relaxed, we have looked for the most energetically convenient configuration varying step by step the values of the two lattice parameters a and c/a, in the same way discussed for α-Ti in section 3.1.

The trends of the crystal energy with respect to different values of the lattice parameters, for all the different functionals adopted in this work, are shown in figures (3.10) and (3.11) and summarized in table (3.4).
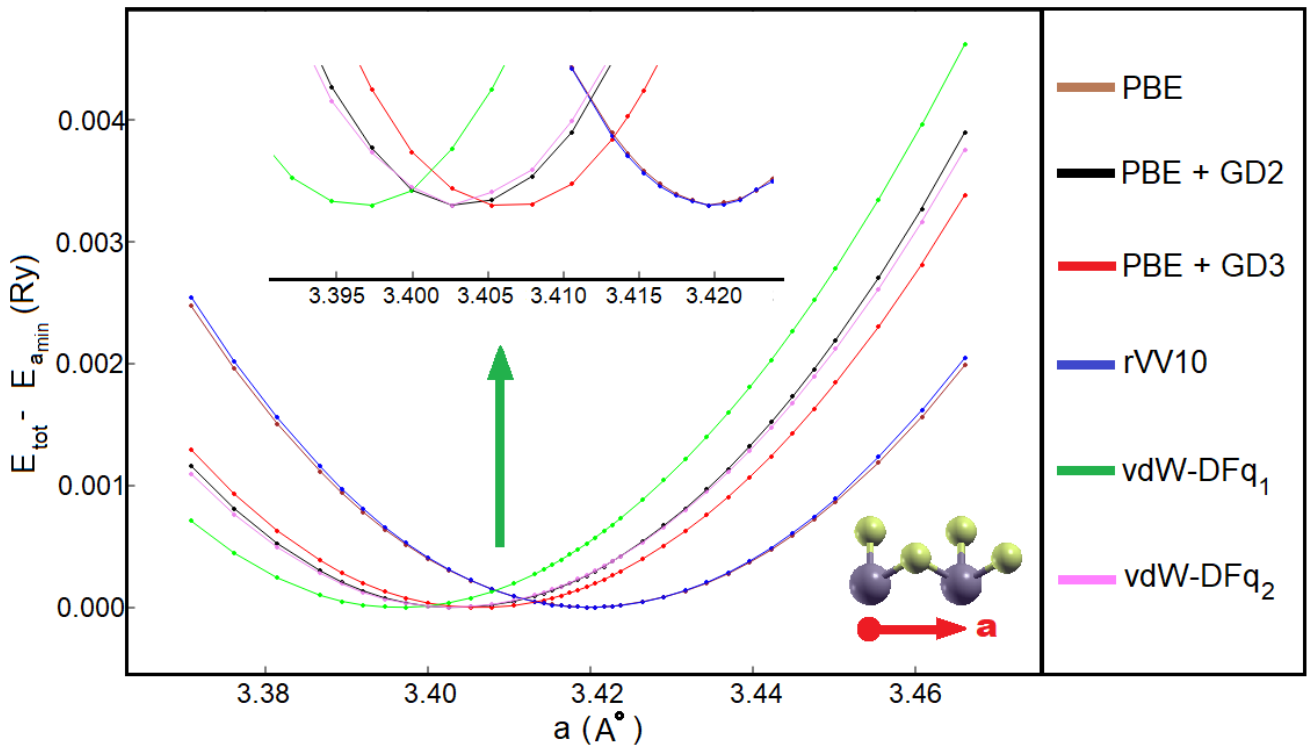

Figure 3.9: Optimization of the hexagonal reticular constant a with different functionals, fixing c/a=1.667. The configuration in which the total energy has a minimum is chosen to be $E = 0$.
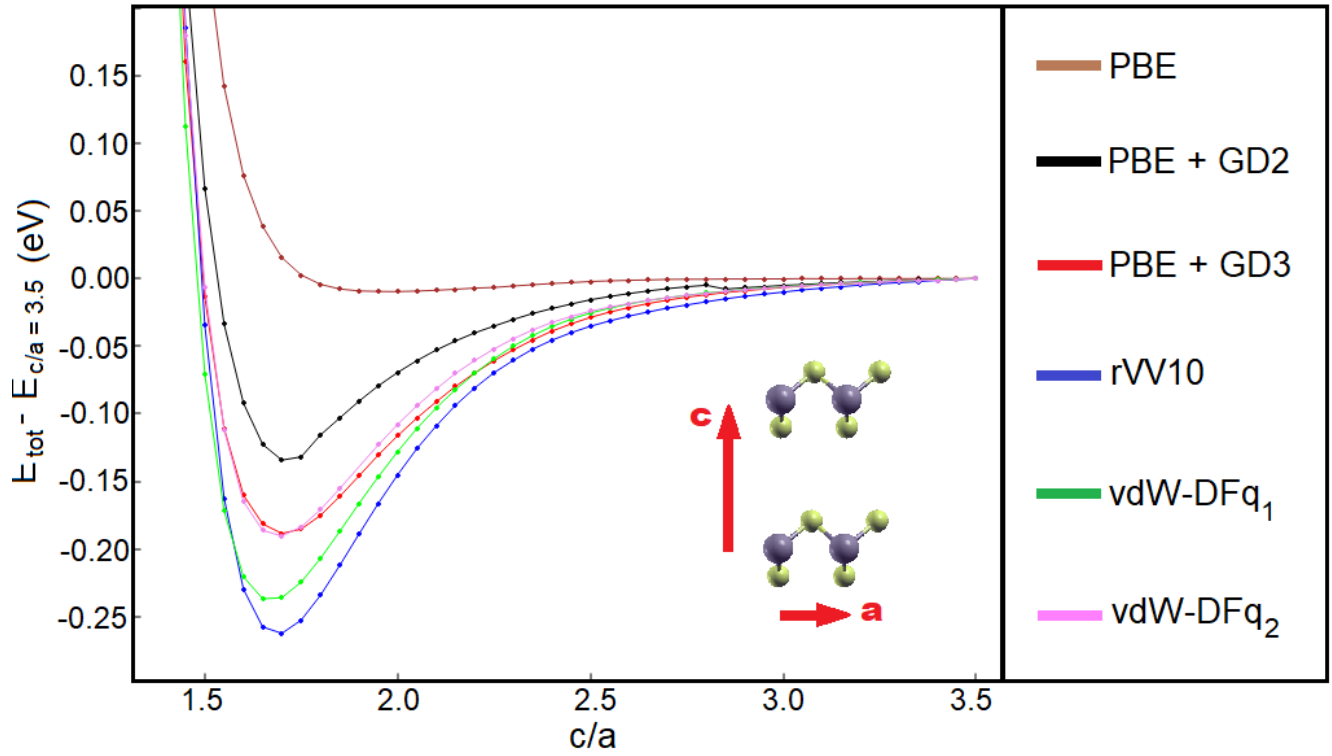
Figure 3.10: Optimization of the longitudinal dimension of the crystal structure through the c/a ratio. Here, the value of a for each functional employed, is fixed to the one that minimizes the energy (i.e. the ones shown in the previous figure).

TiS2 Structural Analysis				
Functional	a (Å)	c/a	Cell Volume(Å)^3	References
PBE	3.419	2.000	69.254	a=3.3976(3) Å [20]
PBE+G-D2	3.403	1.715	58.510	c/a=1.6674 [20]
PBE+G-D3	3.405	1.707	58.370	V=56.6368 Å^3 [20]
rVV10	3.419	1.684	58.313	a=3.4073(2) Å [60]
vdW-DF$q1$	3.397	1.670	56.709	c/a=1.6397 [60]
vdW-DF$q2$	3.403	1.690	57.657	V=56.174 Å^3 [60]

Table 3.4: Summary of the two reticular constants and of the cell volume predicted with the six different functional employed. The literature values of [20] and [60] refer to X-ray diffraction experiments at low temperatures.

- For the hexagonal reticular constant a, all the functionals employed lead to similar results in very good agreement with literature data. The best agreement with the experimental value of ref. [60] is obtained employing **PBE+G-D3**, with an error of only 0.07 %. If comparison is made with the most recent experimental reference [20], the best result is instead obtained using **vdW-DF**q1, with an error of 0.01 %.

  It is interesting to point out that the results obtained employing all the vdW-corrected functionals are really close to the one computed with pure **PBE**, that is a non-vdW-corrected GGA functional. In particular the **PBE** discrepancy is not larger than 0.6 %: this suggests that, as expected, vdW effects are not fundamental in the prediction of the structural properties of TiS_2 on the x-y plane.

- For the c/a ratio, instead, the agreement with literature data is not satisfactory for **PBE**, **PBE+G-D2** and **PBE+G-D3**.

  More specifically, in the case of **PBE**, in which vdW interactions are neglected, the error is of ≈ 19.5 % and ≈ 22 % compared with ref. [60] and ref. [20] respectively. This is a clear signal of the crucial role of vdW interaction in the longitudinal structural features of TiS_2.

  The situation is significantly better, although not optimal yet, employing **PBE+G-D2** and **PBE+G-D3**: in these cases the error is of the order of ≈ 2.5 % and ≈ 4.3 %, again comparing with ref. [60] and ref. [20].

  The reason why the application of these three methods fails is that vdW interactions are the dominating contributions for the longitudinal dimension of the structure and these three functionals are not able to reproduce such effects in a properly correct way. In fact, in the case of a pure GGA (i.e. PBE), vdW effects are basically neglected while, in the cases of this latter coupled with the Grimme's corrections, vdW effects are accounted approximately in a post-processed way and not directly computed adopting a non-local exchange correlation functional, missing, among the other things, genuine many-body correlations and so, leading to unsatisfactory results.

- The unit cell has a volume given by the expression

$$V = a^2 c \sin(120\,°) \,,$$

  the best agreement is obtained with the method **vdW-DF**q1, both with respect to ref. [60] and to ref. [20], the error being respectively ≈ 0.13 % and ≈ 0.95 % if compared with ref. [60] and ref. [20].

  Another reasonable performance is the one obtained with **vdW-DF**q2: in this case the error is ≈ 1.80 % and ≈ 2.64 % with respect to ref. [20] and ref. [60].

Once the most energetically convenient configuration for all the functionals adopted is determined, it is possible to compute the CE and the ILBE.

The first quantity is defined in the following way:

$$CE = E(TiS_2) - E(Ti) - 2E(S) \tag{3.1}$$

where E(Ti) and E(S) are respectively the energies of the isolated Ti and S atoms. Also in this case, as in the one of bulk Titanium treated before, it is important to account for the spin-polarization of the isolated atoms in the ground state. For an isolated S atom a spin-polarized configuration for the ground state is predicted, while for the atomic basis of TiS_2, the computed ground state is spin-less. This is accounted in our calculations of the cohesion energy, in which we have employed the two spin-polarized configurations predicted for the isolated Ti and S atoms.

To ILBE, instead, we are referring to a physical quantity that gives a quantitative estimation of how strong the interalyer interactions are. More specifically, since the main contribution to ILBE is given by vdW interactions, by computing this quantity, we are also able to understand to what extent they are important in the determination of the structural features of this layered material. In practice, computing the ILBE is the same as evaluating the well depth of the potential energy curve, shown in figure (3.11). In principle, to do so, we have to consider the difference $E_{(c/a)_{min}} - E_{c/a=\infty}$ but it is clear that the second factor cannot exactly be computed. For this reason, we approximate $E_{c/a=\infty} \approx E_{c/a=3.5}$, assuming that above this value of the c/a ratio the *interlayer* interactions are negligible.

The results of the energetic analysis are presented in table (3.5).

TiS$_2$ **Energetic Analysis**			
Functional	CE (eV)	ILBE(eV)	References (eV)
PBE	-15.055	-0.010	ILBE:
PBE+G-D2	-15.621	-0.135	[-0.056 ; -0.165] [61]
PBE+G-D3	-15.600	-0.189	CE
rVV10	-15.682	-0.263	[-12.230 ; -20.557] [61]
vdW-DFq1	-16.212	-0.238	CE$_{exp}$:
vdW-DFq2	-15.526	-0.190	-14.746 [61]

Table 3.5: Summary of the values of ILBE and CE for TiS$_2$, computed with the six different functional adopted. The theoretical calculation of the literature data [61] are obtained with Hartree-Fock (**HF**) and corrected-**HF** theories.

- The results for the CE are compatible with both the theoretical and experimental data of [61], even if all of them are overestimating the experimental CE reference. The best agreement is obtained employing a pure **PBE**, with an estimate of 2.1 % above the experimental value but, it is crucial to underline that the configuration in which we have computed the CE is predicted by a GGA scheme that does not properly include vdW interactions and it exhibits a value of the optimized c/a ratio substantially different from the experimental data mentioned. So, the good agreement achieved is most probably due to a compensation of errors in the prediction of the longitudinal structural properties of the material and in the evaluation of the energetic values.

  Therefore, we can safely conclude that the best genuine result, is the one given by **vdW-DF**$q1$, with an error of 5.3 % above the reference value. In any case the good estimate obtained for CE with **PBE** is consistent with the predominant covalent nature which characterizes the intralayer bonds in TiS_2 (this will be discuss in detail in section (3.3.3)).

- The results for the ILBE are also in line with the theoretical data available, although it must be pointed out that these have been obtained using approximate **HF** schemes.

  More specifically, the only one that is inside the reference interval is the value obtained with **PBE+G-D2**. The other vdW-corrected functionals give results slightly above the upper limit of the interval; instead the one achieved with pure **PBE** is slightly below. Looking at the ILBE values plotted in figure (3.11) it is clear that in all the cases (with the exception of **PBE**) there is an appreciable well depth, which means the formation of a weakly bound state induced by the presence of TiS_2 *interlayer* vdW interactions. Interestingly, in the case of pure **PBE** the observed potential energy well depth is almost vanishing and turns out to be too small to permit the formation of a sufficiently stable bulk structure of TiS_2.

  Moreover, if ILBE is computed at the **PBE** level assuming the experimental reticular constants, instead of using the **PBE** parameters, one obtains ILBE=0.033 eV and ILBE=0.047 eV, considering the parameters reported in ref. [20] and [60], respectively. The fact that positive ILBE values are obtained, indicating that the *interlayer* potential is even repulsive, shows again the basic inadequacy of **PBE** to correctly describe *interlayer* interactions, determined by vdW forces.

3.3.2 Electronic band structure of TiS$_2$

In the literature, at it was pointed out above, there are many conflicting results on the electronic structure of TiS$_2$ since it is still debated whether the material is metallic, semimetallic or semiconductor. Several experimental works have reported that TiS$_2$ has a semiconductor behavior with a band gap ranging from 0.05 to 2.5 eV [62]. At the same time, other experiments classify TiS$_2$ among metals [63] or semimetals [64] with an indirect band gap overlap ranging from 0.2 to 1.5 eV The aim of this section is to report the results obtained in theoretical studies of the electronic properties of TiS$_2$ by using both the vdW-corrected functional **vdW-DF**q1 and a pure **PBE** one, in order to appreciate the differences in the electronic band structure induced by vdW interactions. The band structure calculations have been performed following an high-symmetry k-path shown in figure (3.12), to which the following k points belong:

- $(k_x, k_y, k_z)^T = (0, 0, 0)^T \equiv G$

- $(k_x, k_y, k_z)^T = (0, -0.5, 0)^T \equiv M$

- $(k_x, k_y, k_z)^T = (-0.66, 0.33, 0)^T \equiv K$

- $(k_x, k_y, k_z)^T = (0, 0, 0)^T \equiv G$

- $(k_x, k_y, k_z)^T = (0, 0, 0.5)^T \equiv A$

- $(k_x, k_y, k_z)^T = (0, -0.5, 0.5)^T \equiv L$

- $(k_x, k_y, k_z)^T = (-0.66, 0.33, 0.5)^T \equiv H$
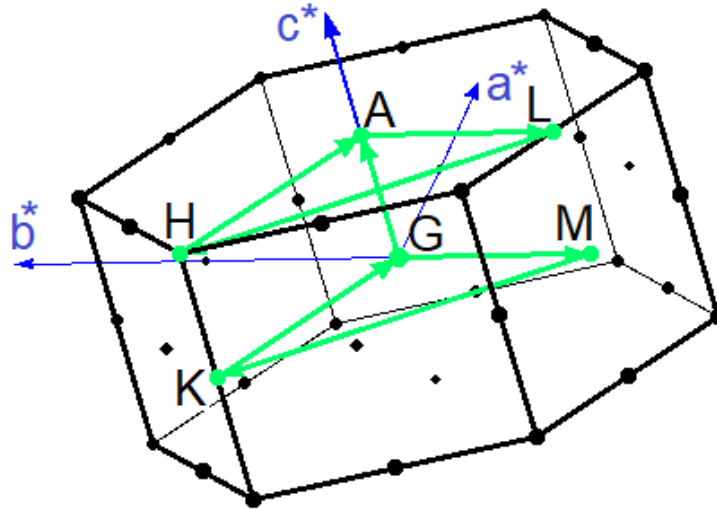
- $(k_x, k_y, k_z)^T = (0, 0, 0)^T \equiv A$

Figure 3.11: k-path for band structure calculations, the electronics eigenvalues are computed for 50 different k values between every high symmetry point of the k path chosen.

To make the analysis more complete and clearly show the positions of the band gaps, total electronic density of states (DOS) calculations are also performed.
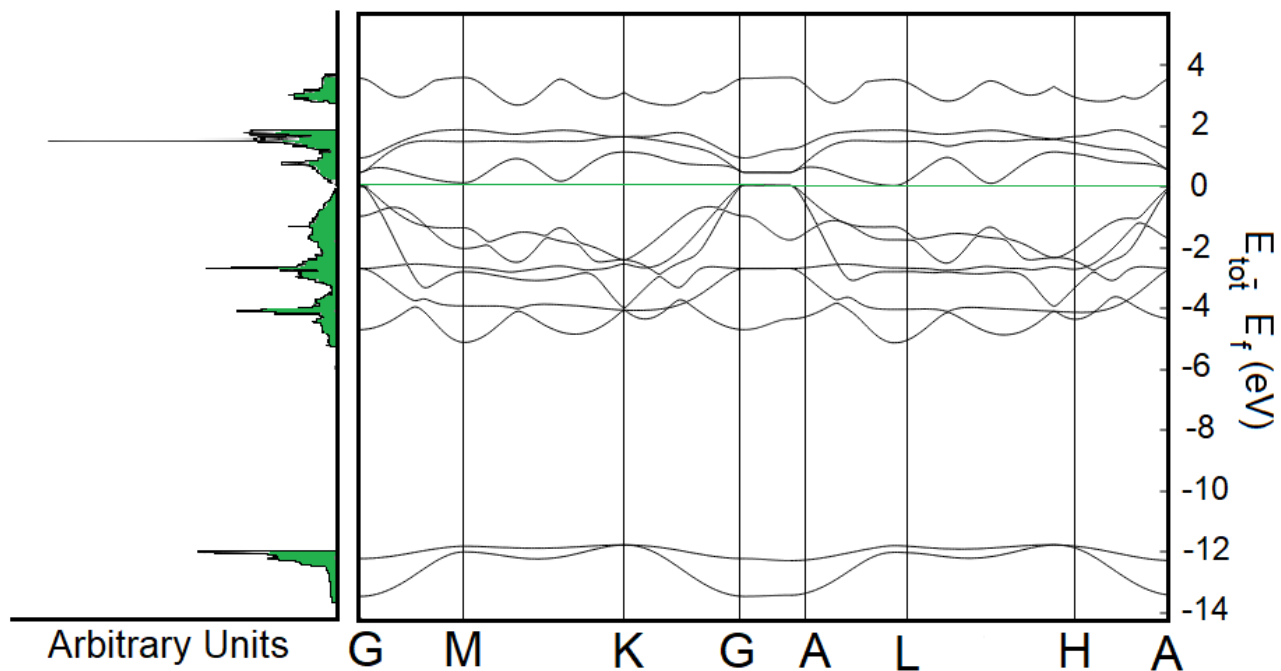
Figure 3.12: Band structure and total electronic DOS computed with pure **PBE**. The Fermi energy E_F=5.451 eV is set to 0.
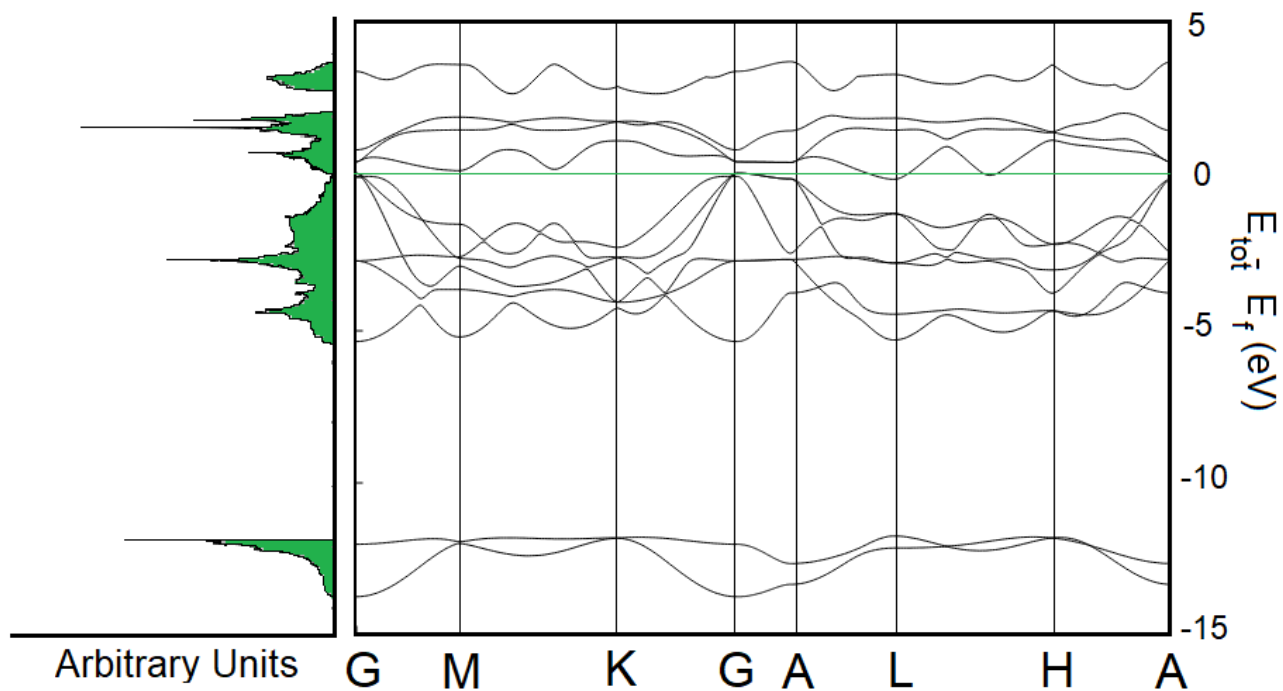

Figure 3.13: Band structure and total electronic DOS computed with **vdW-DF**q1. The Fermi energy E_F=7.874eV is set to 0.

Direct Band Gaps Analysis: PBE ; vdW-DFq1			
k-Point	VB-E_F (eV)	CB-E_F (eV)	Gap (eV)
G	0.031 ; 0.147	0.442 , 0.538	0.411 ; 0.391
M	-1.371 ; -1.524	0.107 ; 0.247	1.478 ; 1.771
K	-2.436 ; -2.285	1.122 ; 1.229	3.558 ; 3.514
A	0.016 ; -0.041	0.440 ; 0.519	0.456 ; 0.560
L	-1.337 ; -1.167	0.010 ; -0.031	1.347 ; 1.198
H	-2.360 ; -2.179	1.125 ; 1.246	3.485 ; 3.425

Table 3.6: Summary of the energies associated to the energy of the valence band (VB), of the conduction band (CB) and relative direct band gaps at the high-symmetry k-points with respect to the Fermi energy E_F.

We have chosen to plot the twelve bands closest to the Fermi level, both for **PBE** and **vdW-DFq1**. The shape observed is similar both for the DOS and for the electronic bands.

We have evaluated the valence band and the conduction band energy at each high symmetry point analyzed, to calculate the associated direct band gaps. Bands gaps computed with **PBE** range from 0.411 to 3.558 eV, the ones predicted with **vdW-DFq1** are instead from 0.391 to 3.514 eV. The gap amplitudes computed using the two functionals are comparable for the **G**,**K**,**H** points, while instead significant differences are found for the **M**,**A**,**L** points: 0.293, 0.104 and 0.149 eV respectively.

Interestingly, while the electronic band structure obtained with **PBE** predicts essentially that TiS$_2$ does not exhibit indirect band gaps (the $\mathbf{A} \to \mathbf{L}$ and the $\mathbf{G} \to \mathbf{L}$ gaps are only 0.006 and 0.021 eV respectively), there is a significant difference by using the **vdW-DFq1** functional, which properly takes the vdW interactions into account. In fact, a $\mathbf{G} \to \mathbf{L}$ indirect band gap of 0.116 eV is observed, supporting the semimetal nature of TiS$_2$, in line with experimental findings [65].

Experimental estimates of the TiS$_2$ indirect band gaps are spread over a wide range, from 0.2 to 1.15 eV (see for example [64]).

Since our **vdW-DFq1** is much closer to the experimental data than **PBE**, and also considering the well-known tendency of DFT calculations to underestimate band gaps [66], we conclude that **vdW-DFq1** allows a much better description of TIS$_2$ than **PBE** and that, also for the electronic band properties, the vdW effects are important, in line with what has been also observed in ionic solids (see ref. [66]).

3.3.3 Analysis of the *interlayer* and *intralayer* electronic charge density

Here we present and compare with literature data the results obtained for the analysis of the electronic charge density distribution both in *intralayer* and *interlayer* regions.
While in the intralayer region the S-Ti bond is strong and covalent in nature, in the *intralayer* one, the S-S bonds are more difficult to characterize due to the presence of weaker vdW interactions.
For each functional, the goal is to evaluate the charge density at the bond critical point (BCP), which is defined as the point along the line connecting two atoms in which the linear charge density reaches a (non-vanishing) minimum value.

intralayer region

For the analysis of the covalent bond of the *intralayer* region we have focused on the portion of space highlighted in figure (3.15)
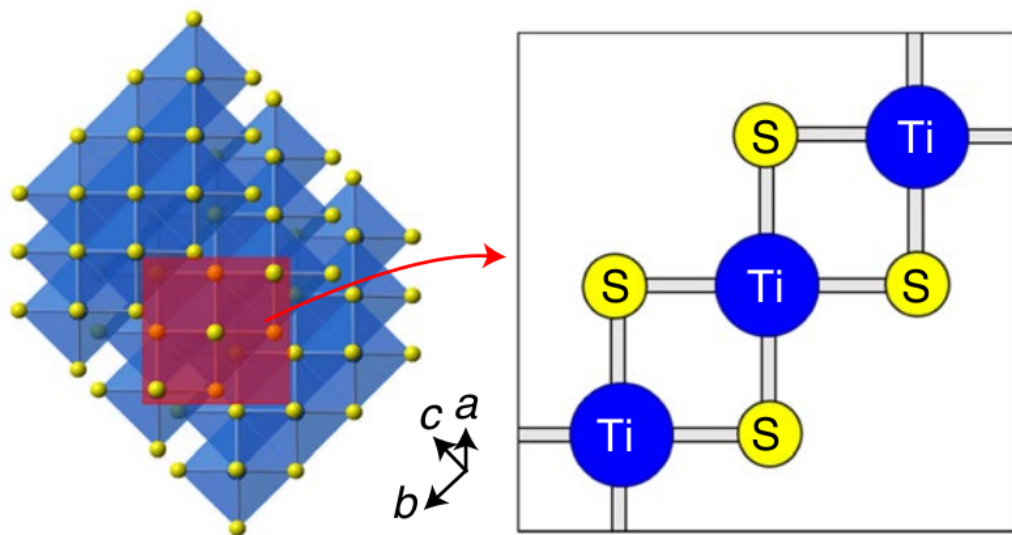

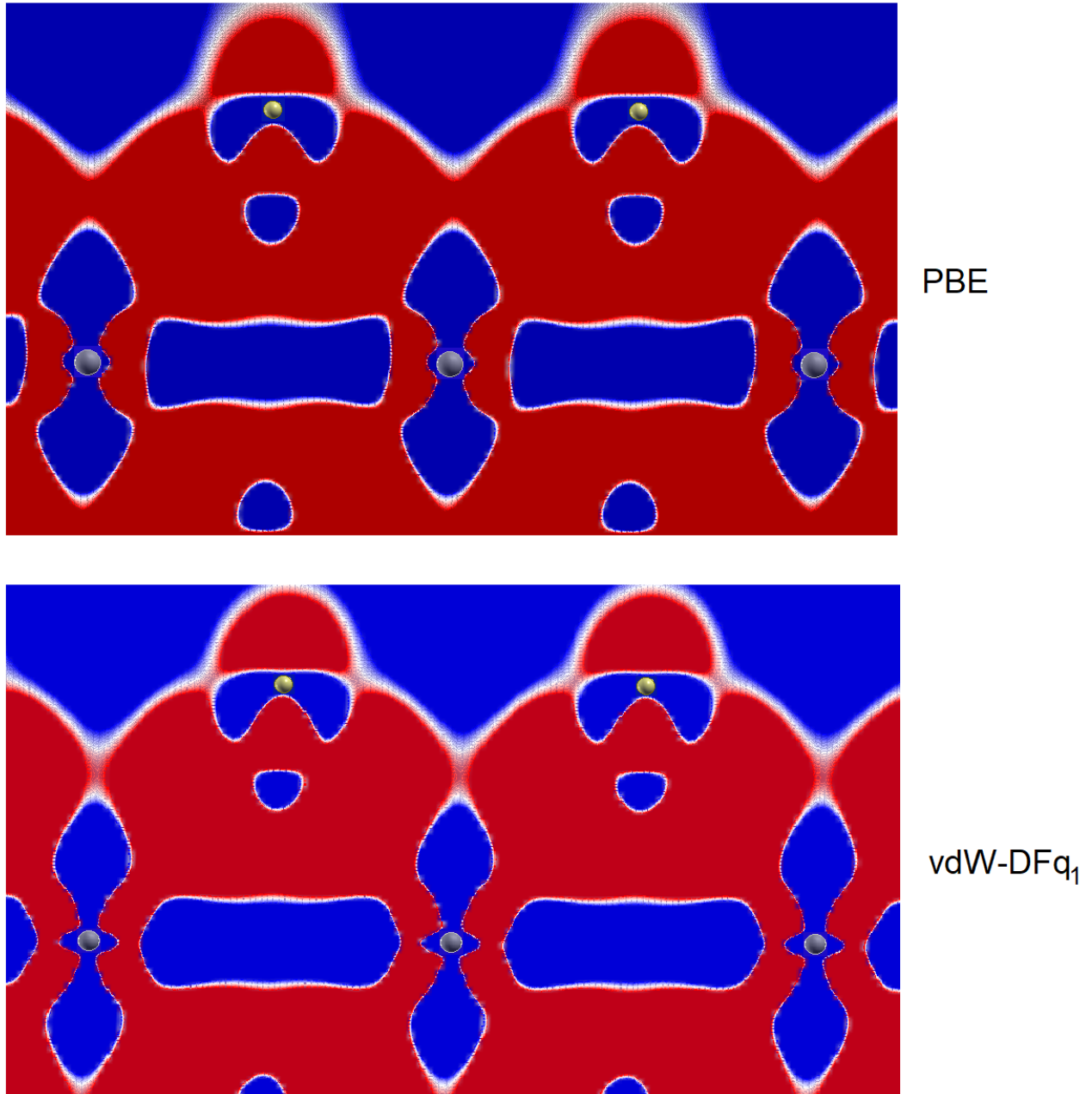Figure 3.14: *Intralayer* region considered for the analysis of the covalent BCP.

Figure 3.15: Profile of the electronic *differential* charge density in the *intralayer* fragment of TiS_2, computed both with **PBE** (top) and with **vdW-DF**$q1$ (bottom) functional.
Such a quantity is defined as $n_{diff} = n(TiS_2) - n(Ti) - n(S_1) - n(S_2)$ (i.e. is the charge density variation due to the presence of the interactions between the atoms), referring to the atoms in their optimized position predicted by the functional employed. Here, the plotting range for n_{diff} is chosen to be [-7.4×10^{-4} ;7.4×10^{-4}] e/ $Å^3$ similarly to ref. [20]. The blue color indicates the regions where there is an electron depletion, the red regions indicate an electron excess, and the white regions are the areas associated to the zero value. With the use of this two different functionals no appreciable differences are apparent.
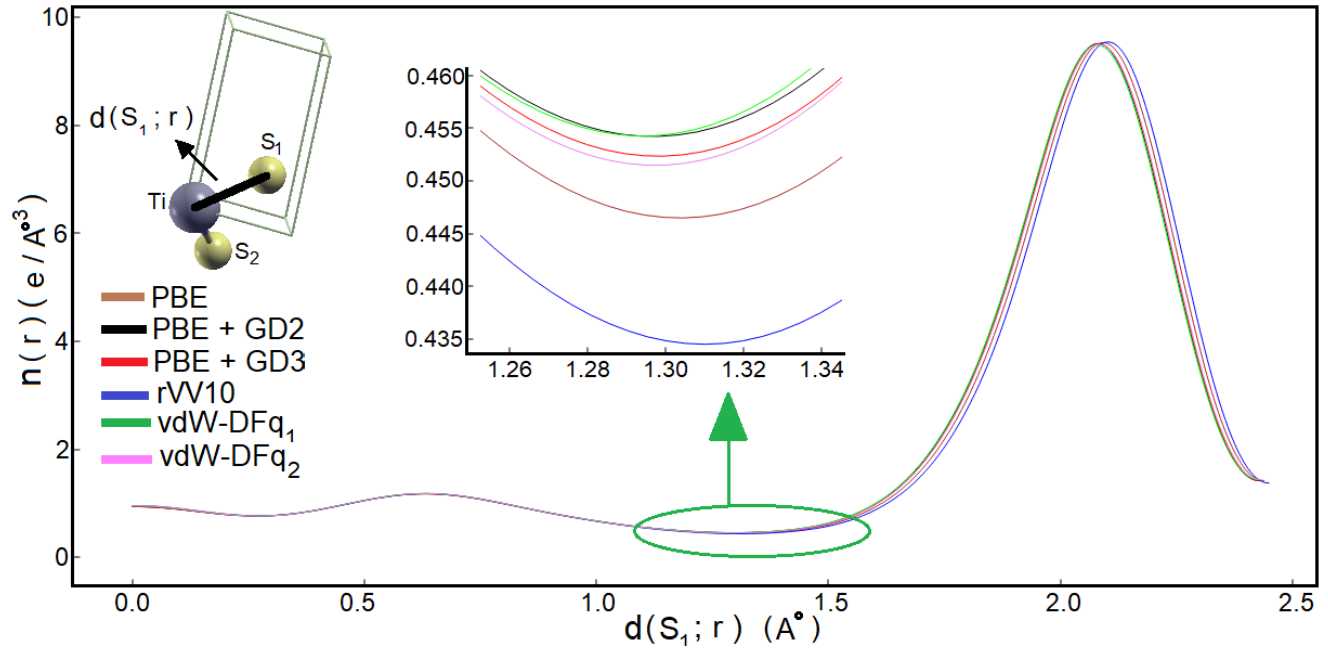
Figure 3.16: Profile of the charge density on the line connecting an S atom (named S_1, on the left side) to a Ti atom (on the right side).

S$_1$-Ti Bond Critical Point Analysis				
Functional	$\rho(r_b)$ e/Å^3	$\rho(r_b)_{REF}$ [20] e/Å^3	d(S$_1$;Ti) Å	d(S$_1$;r_b) Å
PBE	0.447	0.459	2.438	1.304
PBE+G-D2	0.454	-	2.426	1.298
PBE+G-D3	0.452	-	2.429	1.299
rVV10	0.435	0.459	2.449	1.310
vdW-DF$q1$	0.454	-	2.425	1.293
vdW-DF$q2$	0.452	-	2.429	1.295
$\rho(r_b)_{EXP} = 0.429$ [20]				

Table 3.7: Summary of the results for the charge density at the BCP and of the BCP position (r_b) along a line connecting atom S$_1$ and Ti. The structural configurations used for these calculations are the ones considered in table (3.4).

As can be seen, the electronic charge tends to build up around the Ti atom. Moreover, the BCP is located slightly on the right of the S-Ti middle point.

For the case of **PBE** and **rVV10** literature data are available and our values for the electronic density at BCP is in a reasonabe agreement with the theoretical prediction of ref. [20]. In particular, our **PBE** result differs from that of ref. [20] by 2.6 %, while for **rVV10**, the discrepancy is slightly higher: 5.2%. Our results are also close to the experimental data of [20], that reports a value for the charge density at the *intralayer* BCP of 0.429 e/Å^3: in this case, the functional leading to the best agreement is **rVV10**, with an overestimation of only 1.4 %.

In any case, we observe that the shape of the computed profiles of the electronic charge density, does not depend too much on the functional adopted. Our analysis leads, for all the functionals, to results really close to each others, showing that, even if the TiS$_2$ structural predictions of **PBE** are slightly worse (table (3.4)), this does not strongly affect the charge density at BCP for the *intralayer* covalent bonds of TiS$_2$.

This leads to the conclusion that vdW effects do not strongly influence the covalent character of the *intralayer* bonds of TiS$_2$. Note that, if the charge density at the BCP is evaluated at the **PBE** level using the experimental lattice parameters of ref. [20], one obtains $\rho(r_b)$=0.457 e/Å^3, that is a value almost coincident with that reported in ref. [20] (see table (3.7)), thus showing that the small discrepancy between our **PBE** estimate and that of ref. [20] is essentially due to the slightly different **PBE** relaxed parameters.

interlayer fragments

The considered *interlayer* region is highlighted in figure (3.18). By performing the same analysis as in the *intralayer* case, one can observe different interesting features.
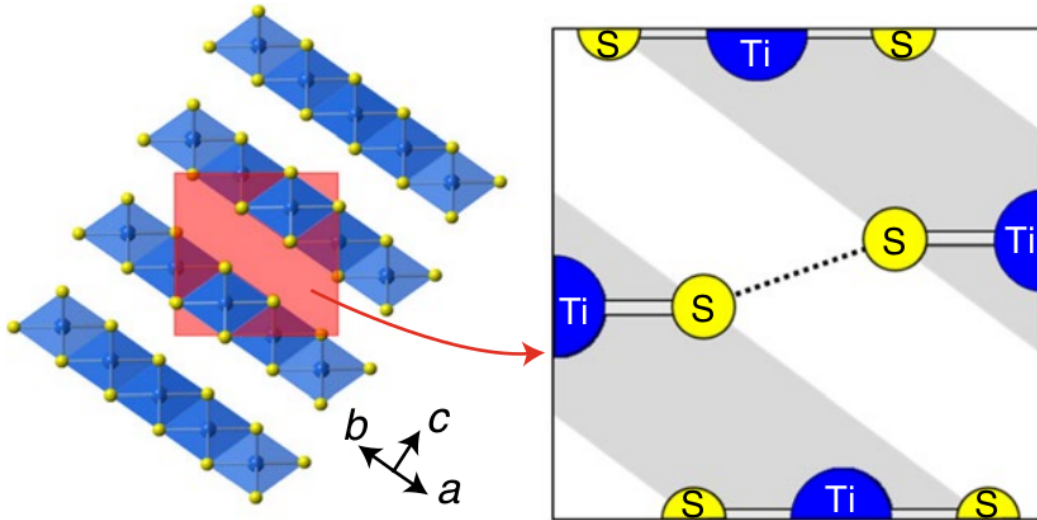

Figure 3.17: *interlayer* region considered for the analysis of the weaker bond characterized by the presence of vdW interactions.
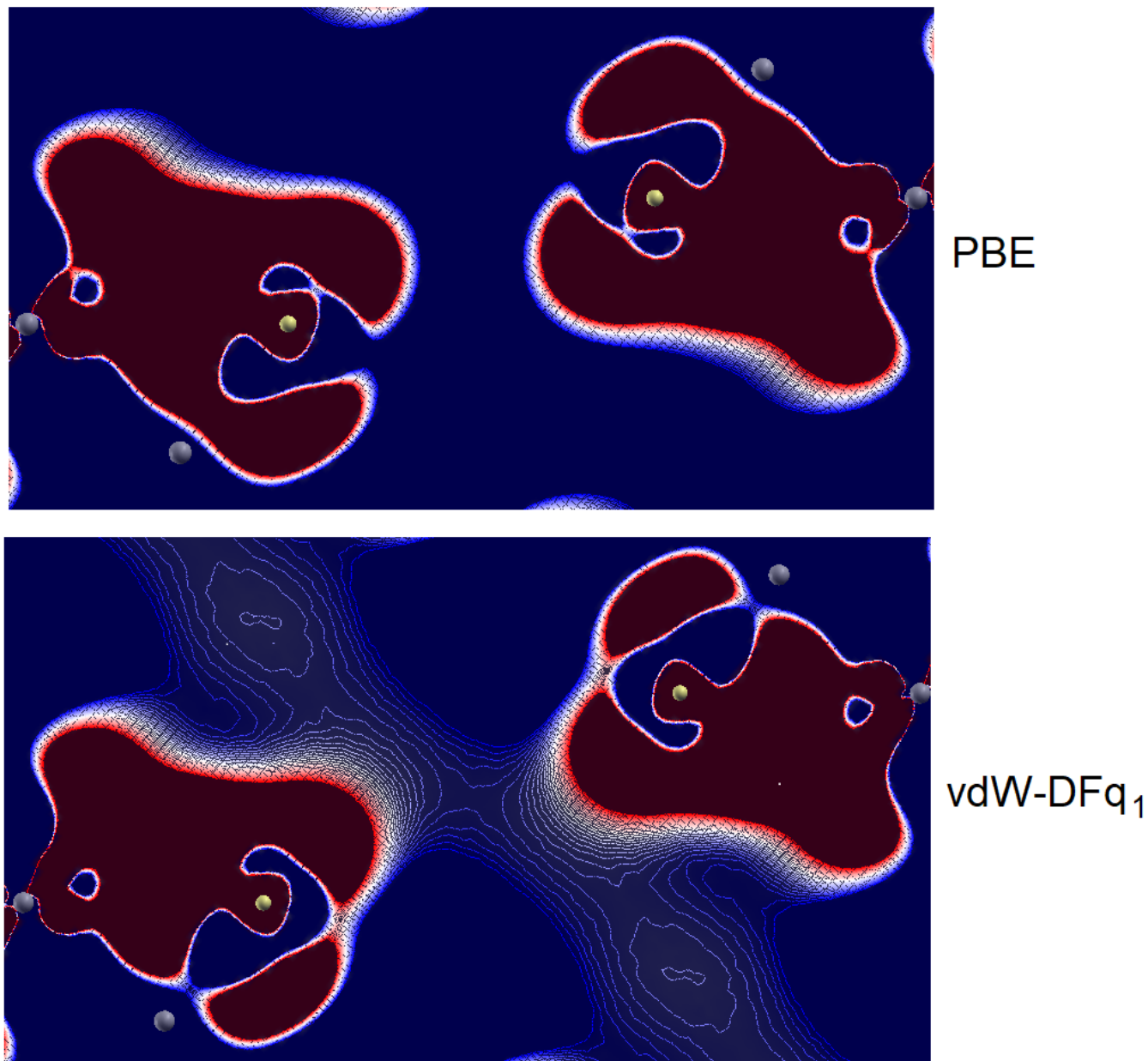
Figure 3.18: Profile of the *differential* electronic charge density in the *interlayer* region of TiS_2, computed both with **PBE** (top) and with **vdW-DF**$q1$ (bottom) functional. For consistency with the *intralayer* case, the plotting range is chosen to be again [-7.4×10^{-4} ; 7.4×10^{-4}] e/$\mathring{A}^3$. The color scheme is the same as that adopted in figure (3.16). The incomplete depletion of the electronic charge in the region between the two S atoms, obtained by **vdW-DF**$q1$, differently from **PBE**, can support the formation of a weak S-S bond due to the vdW interactions which are taken into account by **vdW-DF**$q1$.
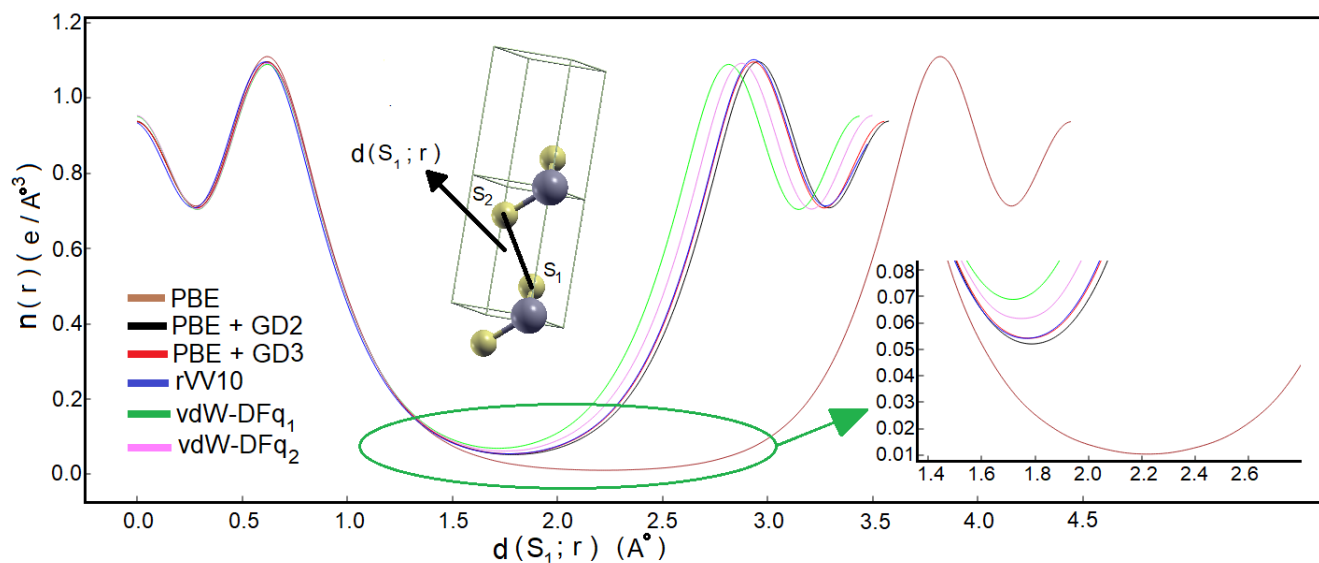
Figure 3.19: Profile of the charge density on the line connecting a S atom (named S_1, on the left side) to another S atom (named S_2, on the right side).
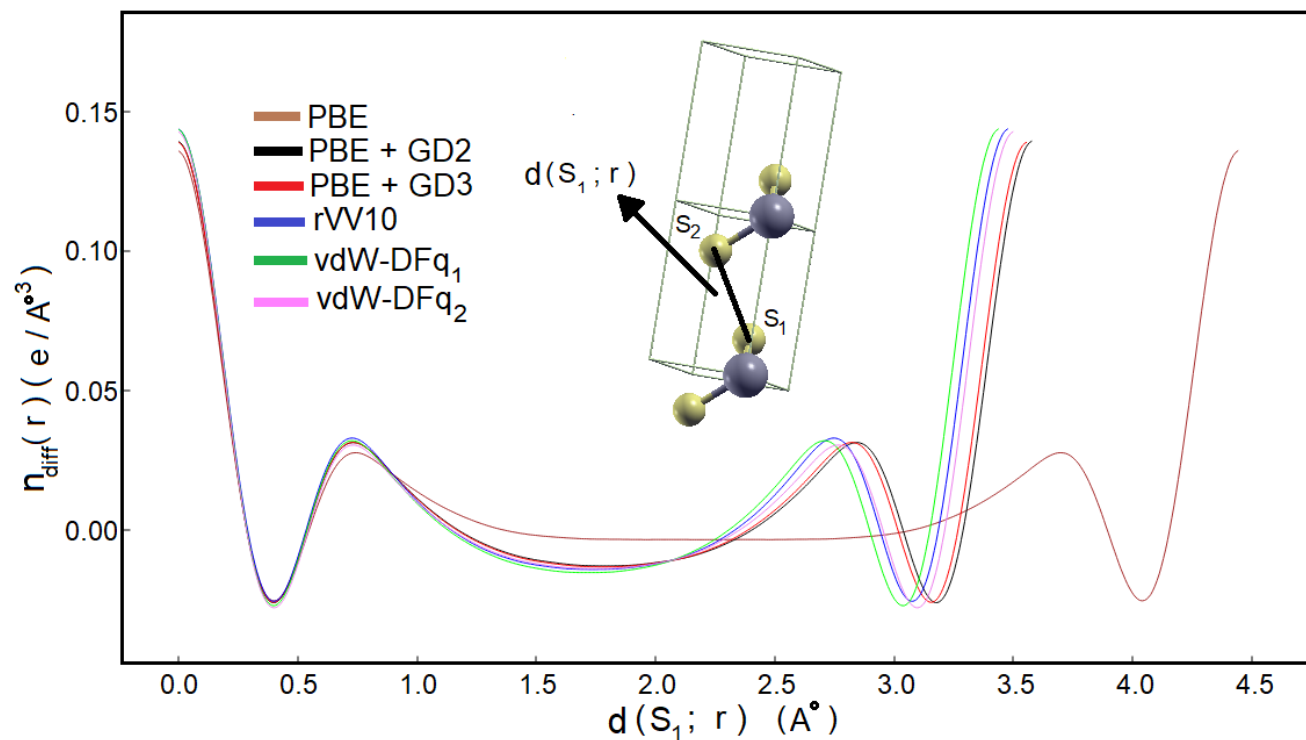

Figure 3.20: Profile of the *differential* charge density on the line connecting a S atom (named S_1, on the left side) to another S atom (named S_2, on the right side).

S_1-S_2 Bond Critical Point Analysis				
Functional	$\rho(r_b)$ e/Å^3	$\rho(r_b)_{REF}$ [20] e/Å^3	d(S_1;S_2) Å	d(S_1;r_b) Å
PBE	0.010	0.0670	4.442	2.220
PBE+G-D2	0.052	-	3.575	1.791
PBE+G-D3	0.054	-	3.554	1.780
rVV10	0.054	0.0680	3.476	1.793
vdW-DFq1	0.069	-	3.436	1.722
vdW-DFq2	0.062	-	3.497	1.745
$\rho(r_b)_{EXP} = 0.086$ [20]				

Table 3.8: Summary of the results for the charge density at the BCP and of the BCP position (r_b) along a line connecting atom S_1 and S_2. The structural configurations used for these calculations are the ones considered in table (3.4).

As can be seen in figure (3.20) the *interlayer* charge density between the two S atoms is almost perfectly symmetric.

Remarkable, using **PBE**, the charge density at the BCP position is much smaller than the corresponding values obtained by the other functionals. This can be easily understood recalling (see table (3.4)) that the c/a ratio predicted by **PBE** was significantly larger than both the experimental estimates and the values obtained by the other functionals. It is therefore reasonable that if the *interlayer* distance is overestimated, this leads to a pronounced reduction of the electronic charge density in the *interlayer* region. Moreover, as we have also pointed out, vdW interactions (not properly described by **PBE**) affect not only the basic structural *interlayer* parameter of TiS$_2$, but also the electronic band structure.

Note that our **PBE** charge density at BCP is much smaller than the **PBE** value reported in ref. [20]. This discrepancy can be explained by the fact that in ref. [20] the experimental c/a ratio was considered, while in our case we have used the c/a ratio optimized by **PBE**, which is certainly a more consistent approach. In fact, if $\rho(r_b)$ at the *interlayer* BCP is recomputed, within a **PBE** scheme, using the lattice constants of ref. [20], we obtain $\rho(r_b)$= 0.0673 e/Å^3, that is a value very close to the **PBE** estimate reported in ref. [20].

Note that the estimate is also similar to the values found with the other vdW-corrected functionals: this agreement is entirely due to the inconsistent choice of forcing the *interlayer* distance to be much shorter than **PBE** predicts, again indicating the inadequacy of **PBE** to take vdW effects into account.

Using instead the vdW-corrected **rVV10** functional, we find a BCP charge density not far from the **rVV10** value reported in ref. [20]. Probably we get a lower-value estimate because of a slightly larger c/a ratio obtained at the **rVV10** level (see table (3.4)).

Interestingly, the BCP charge densities obtained using the **vdW-DFq1** and **vdW-DFq2** functionals are closer to both the **rVV10** value of ref. [20] and to the experimental finding [20]. In particular **vdW-DFq1** turns out to give the best result, although even the **vdW-DFq1** BCP density is about 20% smaller than the experimental estimate reported in table (3.8). This indicates that **vdW-DFq1** improves the **rVV10** performance but it does not seem to be able to fix the basic discrepancy existing between theoretical and experimental electron-charge densities mentioned in

the Introduction section.

3.3.4   Tuning of the q parameters in the vdW-DFq functional

In ref. [45], a tuning of the q parameter of the original Hamada functional (**vdW-DF$q1$**) for the optimization of the mass density in semi-hard material was proposed. Following the same strategy, an interesting development could be to optimize the same parameter in order to make the electronic charge density at the BCP position as close to the experimental estimate as possible. In ref. [20], Kasai et co-workers pointed out that the underestimate of the charge deformation in the *interlayer* fragments of TiS$_2$ is due to the unsuitability of the vdW-corrected functionals nowadays available. Therefore, if one could generate a new vdW-corrected functional able to better describe the *interlayer* charge density, this will probably represent a significant progress towards a more accurate theoretical description of TiS$_2$.

After a set of preliminary test calculations in which we have tried to correct the tendency of the *interlayer* charge density at BCP to underestimate the experimental value, we have chosen to set the value of the new parameter to $q_3{=}0.55$. Employing this new functional, which we term **vdW.DF$q3$**, we have performed an analysis where we evaluate lattice constants, CE, ILBE and the electronic charge density of TiS$_2$, finding a substantial improvement of the electronic density at BCP with respect to the results obtained with the other functionals employed up to now.
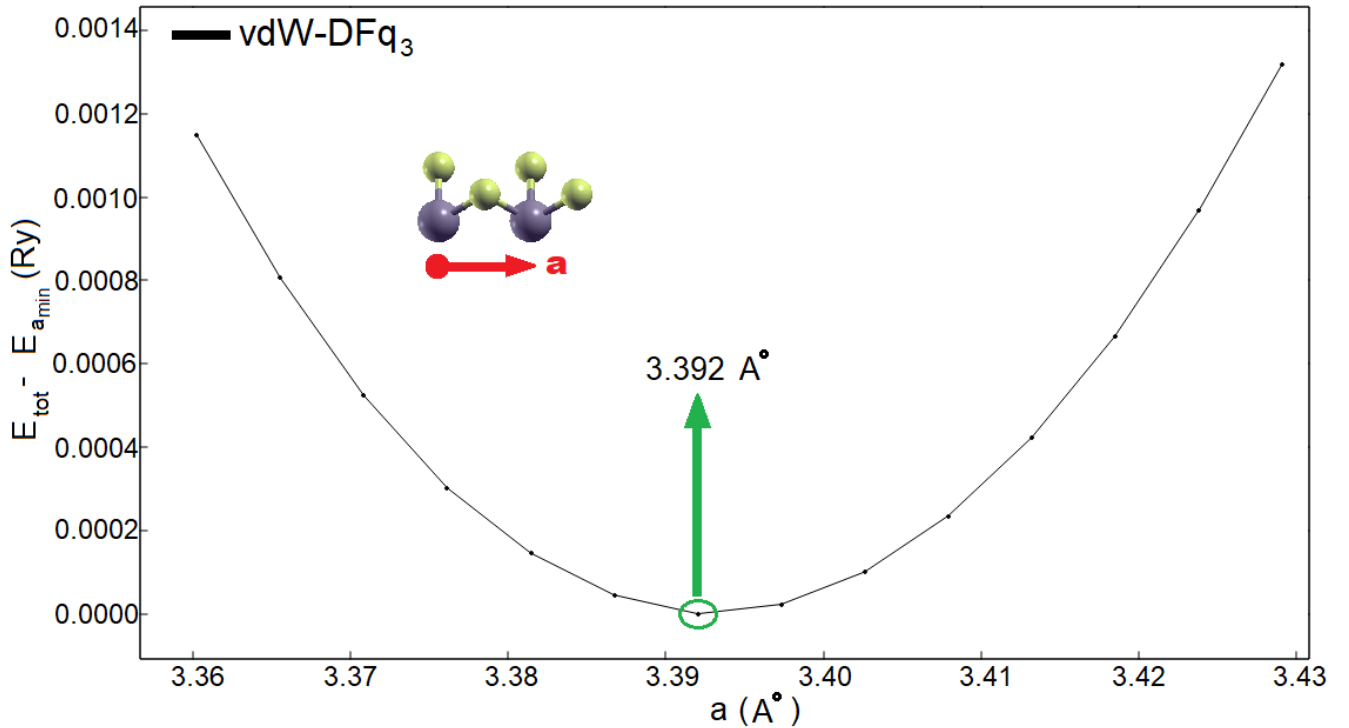

Figure 3.21: Optimization of the hexagonal reticular constant a employing **vdW-DF$q3$**, at $c/a{=}1.667$, according to ref. [20]. The configuration in which the total energy has a minimum is chosen to be $E = 0$.
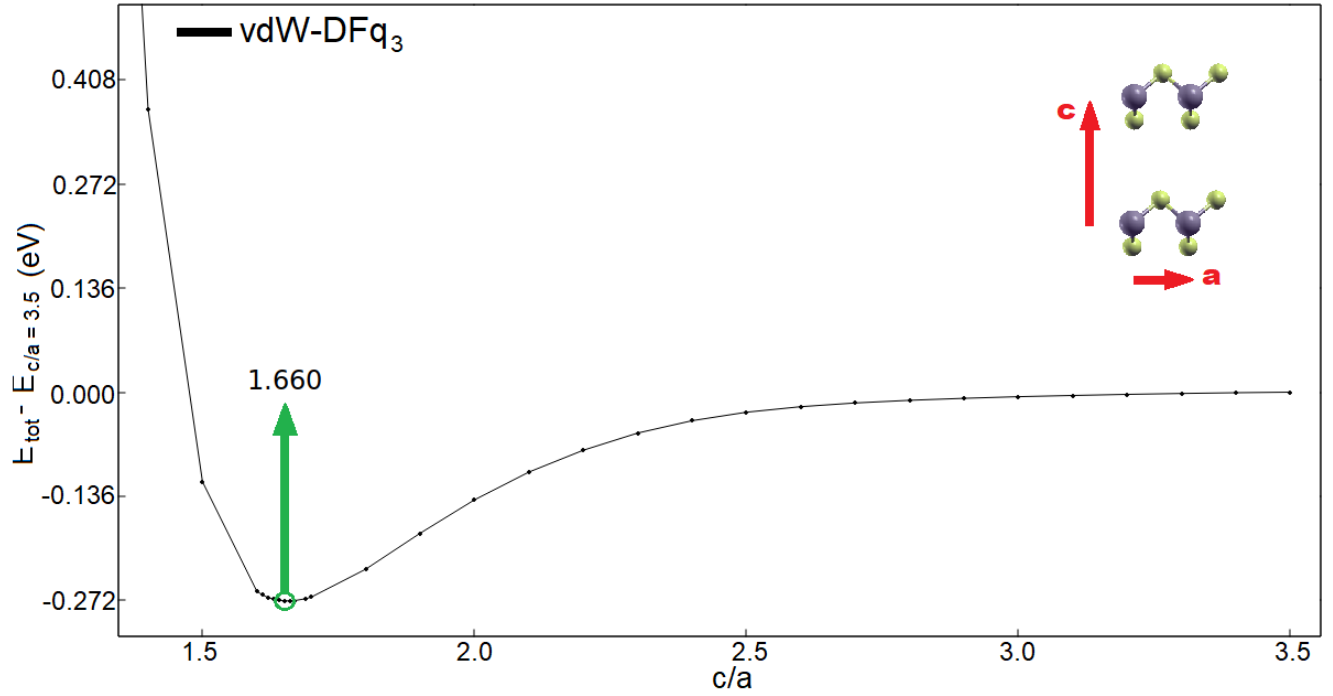
Figure 3.22: Optimization of the longitudinal dimension of the crystal structure through the c/a ratio. Here, the value of a is 3.392 Å, that is the one associated to the minimum energy configuration computed in the previous step.

TiS2 Structural Analysis			
Functional	a (Å)	c/a	Cell Volume(Å)^3
vdW-DF$q3$	3.392	1.660	56.106

Table 3.9: Summary of the structural properties of TiS$_2$ computed with our **vdW-DF**$q3$ functional.

TiS$_2$ Energetic Analysis		
Functional	CE (eV)	ILBE(eV)
vdW-DF$q3$	-16.533	-0.273

Table 3.10: Summary of the energetic properties of TiS$_2$ computed at the lowest energy configuration predicted by our **vdW-DF**$q3$ functional.

The structural result obtained with **vdW-DF**$q3$ are in an extremely good agreement with experimental data of [20] and [60] (see table (3.4)).
In particular, the hexagonal lattice parameter a is only 0.2 % below the one of ref. [20] and 0.5 % below the one reported by ref. [60].
The c/a ratio is 0.4 % below that of ref. [20] and slightly above that of [60], with a discrepancy of just 1.4 %.
vdW-DF$q3$ also improves the estimate of the unit cell volume, since this is just 0.94 % below the

experimental value of ref. [20] and just 1.21 % below the estimate of ref. [60].
However, the same it is not true for the CE and ILBE. More specifically, the prediction of the
cohesion energy is slightly worsened if compared with the experimental data of ref. [61], with
an error of 12.12 %. The result obtained with the original Hamada functional **vdW-DFq1** has
instead an error of only 5.29 % (see table (3.5)).
Moreover, the ILBE value predicted by **vdW-DFq3** is in a worse agreement with the experimental
estimates than the values obtained by the other functionals (see table (3.5)).
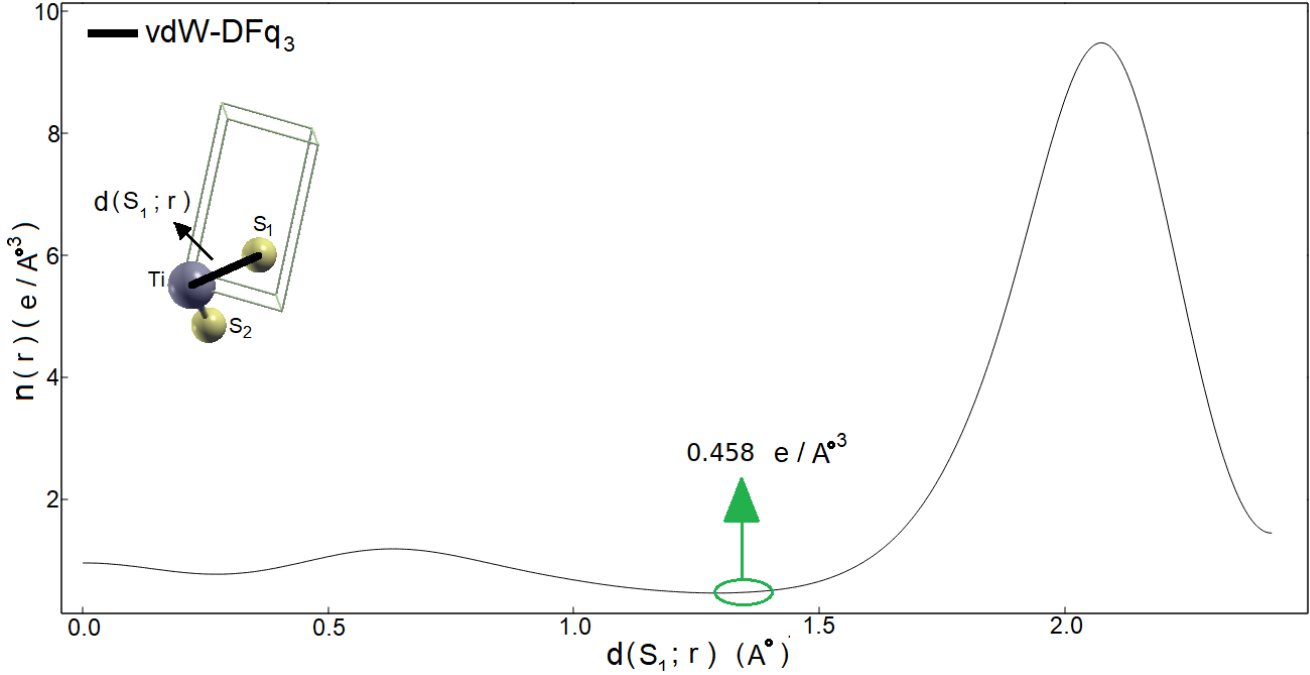

Figure 3.23: Profile of the charge density on the line connecting an S atom (named S_1, on the left side)
to a Ti atom (on the right side), computed with **vdW-DFq3**.

S_1-Ti Bond Critical Point Analysis			
Functional	$\rho(r_b)$ e/Å^3	d(S_1;Ti) Å	d(S_1;r_b) Å
vdW-DFq3	0.458	2.421	1.290

Table 3.11: Analysis of the *intralayer* BCP charge density obtained with **vdW-DFq3** functional.

S_1-S_2 Bond Critical Point Analysis			
Functional	$\rho(r_b)$ e/Å^3	d(S_1;S_2) Å	d(S_1;r_b) Å
vdW-DFq3	0.073	3.406	1.706

Table 3.12: Analysis of the *interlayer* BCP performed with **vdW-DFq3** functional.

The linear density profile computed with the **vdW-DFq3** functional is similar to the ones obtained
by the other functional employed. Comparing with data of table (3.7), the theoretical predictions
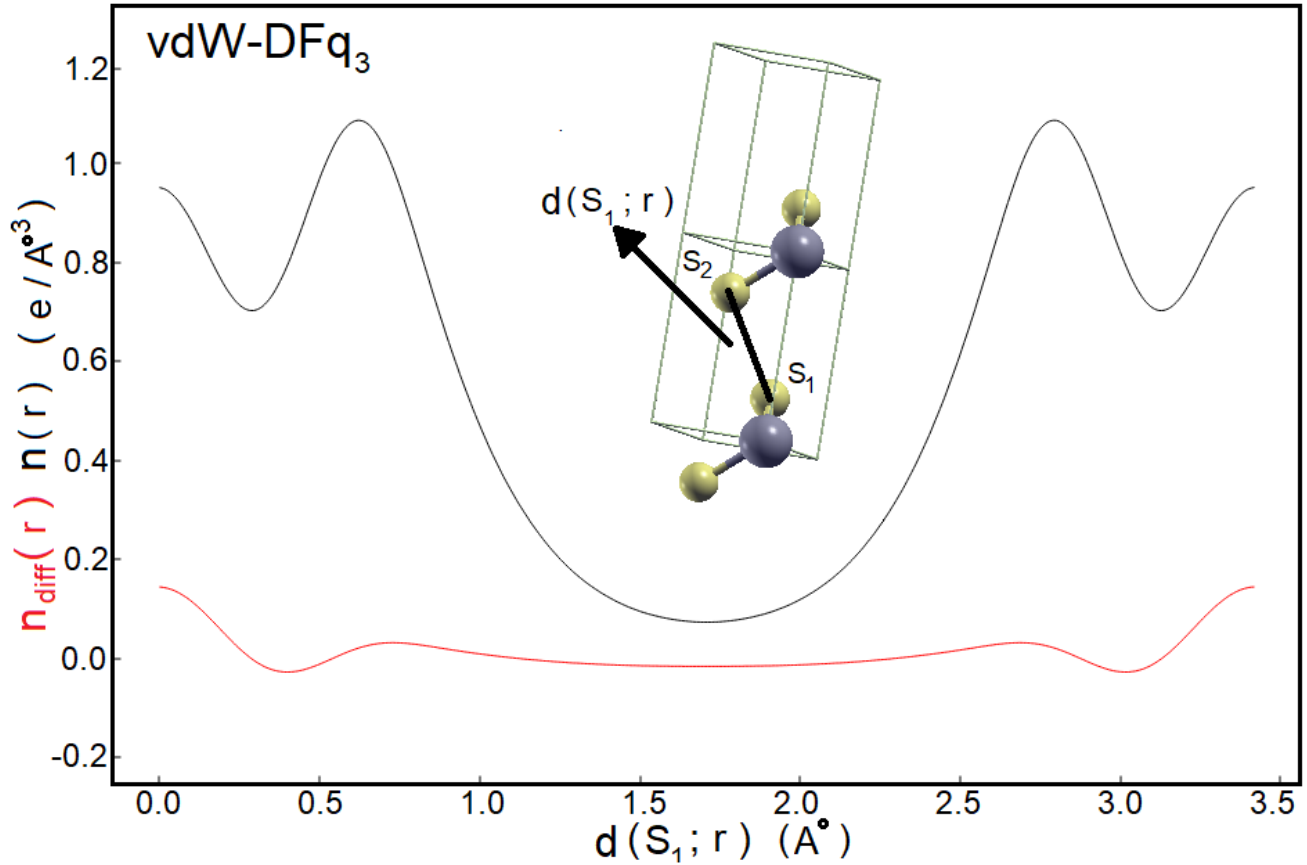
Figure 3.24: Profile of the electronic charge density in the S_1-S_2 *interlayer* region and associated differential charge density, computed with **vdW-DFq3**.

of **vdW-DFq3** for the charge density at the *intralayer* BCP are worse. In fact, for instance, the result obtained with **rVV10** is overestimated by 1.4 %, while the one computed with **vdW-DFq3** is 6.8 % above the experimental result.

The situation is definitely better for the characterization of the S_1-S_2 *interlayer* chemical bonding. In fact **vdW-DFq3** predicts a value of the charge density at BCP of 0.073 e/$Å^3$, thus reducing the discrepancy with respect to the experimental estimate (0.086 e/$Å^3$) from about 20 % (as obtained by the **vdW-DFq1** approach, see table (3.8)) to about 15 %. Therefore, the choice of the new q3 parameter leads to an increase of the electronic charge density at the BCP in the *interlayer* region, in better agreement with the experiment.

3.4 Conclusions and Perspectives

In conclusion, we can summarize the basic results obtained from our detailed structural, energetic and electronic analysis of TiS_2 at T=0, as follows:

- Concerning structural properties, the **PBE** functional (where a genuine description of vdW interactions is missing) fails to predict a reasonable c/a parameter, that is the basic feature of the interlayer bonding.
  Instead, vdW-corrected functionals give much better results, with the best performances obtained using newly proposed **vdW-DF**$q3$ functionals. Very good results are also obtained employing **vdW-DF**$q1$, **vdW-DF**$q2$ and **rVV10**. In particular, by looking at the unit cell volume, **vdW-DF**$q3$, namely our revised version of the original functional of Hamada (see sections (2.2.4) and (3.3.4)), performs slightly better than the **vdW-DF**$q2$ functional, introduced in [45]. This does not come to a surprise. In fact, the $q2$ parameter of ref. [45] was optimized by considering a given set of systems (included some layered vdW materials different from TiS_2) so that one cannot expect that q_2 necessarily improves the description of a specific system, such as TiS_2 which does not belong to the reference set.

- As far as the cohesion energy is concerned, we have found reasonably good results both in the case of the α-Ti (see table (3.2)) and in the case of TiS_2 (see table (3.5)). In particular, considering the result for α-Ti, achieved within a **PBE** approach and the **vdW-DF**$q1$ result for TiS_2, we have an error with experimental data that remains around 5 %.

- Concerning the electronic band structure we have found an interesting effect due to the inclusion of vdW interaction. Employing **PBE**, TiS_2 does not exhibit appreciable indirect band gap, resulting essentially gap-less. Instead, when the **vdW-DF**$q1$ approach is adopted the electronic nature of the material exhibit a substantial variation, showing an appreciable indirect band gap of 0.116 eV (see section (3.3.2)). Within this last scheme, we can conclude that the presence of vdW interactions allow us to characterize TiS_2 as a semimetal, in line with a wide set of experimental references (see for instance [64] and [65]).
  To improve the description of the electronic band structure, it could be useful to compute a partial electronic DOS of Ti and S, in order to split the contributions of the different valence electronic orbitals ($4s$ and $3d$ for Ti, $3s$ and $3p$ for S). This could be useful to observe where the atomic orbitals of Ti and S overlaps, thus giving a more complete description of the orbital ibridization responsible for the strong covalent bond typical of the *intralayers* interactions.
  Moreover, in perspective, it could be interesting to perform band structure calculations employing experimental lattice parameters of TiS_2 subjected to high external pressure. This can be done in the spirit to characterize the semiconductor-semimetal phase transition of TiS_2, that is an issue already mentioned in other studies (see for example in ref. [61]).

- The results for the *intralayer* and *interlayer* electronic charge density distributions are promising, with a wide margin of improving in accuracy.
  In the *intralayer* case (see table (3.7)), **rVV10** exhibits a very good performance, overestimating only by ≈ 1.5 % the experimental charge density at BCP. **vdW-DF**q1 and **vdW-DF**q2 functionals instead perform slightly worse, showing a discrepance of ≈ 5.8 %.
  Regarding the *interlayer* S-S bonding, that is the physical quantity we have decided to take more emphasis on, the **vdW-DF**q approach is the one that has reached the best agreement with the experimental data of ref. [20]. In particular, for the prediction of the charge density at BCP for the weak *interlayer* bonding, the original **vdW-DF**q1 of Hamada has performed slightly better than**rVV10** (see table (3.8)) but, anyway leading to a result of insufficient accuracy, in line with the conclusions of ref. [20].
  Our findings indicate that, differently from the intralayer case, the charge density at the *interlayer* BCP is strongly influenced by the structural features, since our **PBE** estimation is 5-7 times smaller than the ones predicted with the other vdW-corrected functionals.
  The tuning procedure of the q parameter presented in section (3.3.4) seems to be a promising way to improve these results. This is supported by the analysis performed employing our **vdW-DF**q3 scheme, in which we have reached a significantly better result for the *interlayer* charge density at BCP, overcoming the performance of the original **vdW-DF**q1 functional. However, this improvement is achieved at the price of a deterioration in the description of the *intralayer* charge density and of the CE. This seems to indicate that more extended test calculations are required to find an optimal q-parameter, able to allow for a better overall description of the structural, energetic and electronic properties of TiS_2, possibly combined with the research of alternative functional forms.

Chapter 4

Bibliography

[1] Whittingham M. S., "Lithium batteries and cathode materials", Chem. Rev., **104**, 4271, (2004).

[2] Imai H., Shimakawa Y., Kubo Y., "Large thermoelectric power factor in TiS_2 crystal with nearly stoichiometric composition", Phys. Rev. B, **64**, 241104, (2001).

[3] Li Y. et al., "MoS_2 nanoparticles grown on graphene: an advanced catalyst for the hydrogen evolution reaction", J. Am. Chem. Soc., **133**, 7296, (2011).

[4] Hasan M. Z. & Kane C. L., "Colloquium: topological insulators", Rev. Mod.Phys., **82**, 3045, (2010).

[5] Gamble F. R., DiSalvo F. J., Klemm R. A., & Geballe T. H., "Superconductivity in layered structure organometallic crystals", Science, **168**, 568, (1970).

[6] Wilson J. A., Di Salvo F. J., Mahajan S, "Charge-density waves and superlattices in the metallic layered transition metal dichalcogenides", Adv. Phys, **24**, 117, (1975).

[7] Coleman J. N. et al., "Two-dimensional nanosheets produced by liquid exfoliation of layered materials", Science, **331**, 568, (2011).

[8] Chhowalla M. et al., "The chemistry of two-dimensional layered transition metal dichalcogenide nanosheets", Nat. Chem., **5**, 263, (2013).

[9] Geim A. K. & Grigorieva I. V, "Van der Waals heterostructures", Nature, **499**, 419, (2013).

[10] Berland K. et al, "Van der Waals forces in density functional theory: a review of the vdW-DF method", Rep. Prog. Phys, **78**, 066501, (2015).

[11] Filsø M. Ø. et al., "Atomic and electronic structure transformations in SnS_2 at high pressures: a joint single crystal X-ray diffraction and DFT study", Dalton Trans, **45**, 3798, (2016).

[12] Le N. B., Huan T. D., Woods L. M, "*interlayer* interactions in van der Waals heterostructures:

electron and phonon properties", ACS Appl. Mater, **8**, 6286, (2016).

[13] Klipstein P.C. & Friend R.H.J, Phys. C: Solid State Phys, **17**, 2713, (1984).

[14] Trevey J. E., Stoldt C. R., Lee S.-H, "High power nanocomposite TiS_2 cathodes for all-solid-state lithium batteries", J. Electrochem. Soc., **158**, A1282, (2011).

[15] Baresel D. et al., "Ubergangs-Metallchalkogenide als Sauerstoff-Katalysatoren fur Brennstof-fzellen", J. Ber. BunsenGes. Phys. Chem., **78**, 608, (1974).

[16] Atlantic Richfield Co. Neth. Appl. 75 02,156 (Cl. C07C, B01J), (1975), U.S. Appl. 459998, 11 Apr 1974.

[17] Price J. A., Stewart M.J., U.S. 3644291 (Cl. 260-75R; c08G), 22 Feb 1972, Appl. 777460, 20 Nov 1968.

[18] Golub J. et al., "Thermal conversions of dodecacarbonyltriiron on the surface of titanium and molybdenum disulfides", Russ. Chem. Bull., **41**, 32, (1992).

[19] Farr S. et al., "Electrochemical lubrication in the warm working of metals", Lubr. Eng., **36**, 586, (1980).

[20] Kasai H. et al., "X-ray electronc density investigation of chemical bonding in van der Waals materials", Nature Materials, **17**, 249, (2018).

[21] https://www.quantum-espresso.org/full-ref.

[22] Hohenberg P. & Walter K., "Inhomogeneous electron gas", Phys. Rev., **136**, B864, (1964).

[23] Walter K. & Sham Lu Jeu, "Self-Consistent Equations Including Exchange and Correlation Effects", Phys. Rev., **140**, A1133, (1965).

[24] Fetter A. L. ,Walecka J. D. (1971) "Quantum theory of many-particle system" Dover Edition, Ch. 4 "Fermi system", Section 12 "Degenerate electron gas".

[25] Ceperley D. M. & Alder B. J., "Ground State of the Electron Gas by a Stochastic Method", Phys. Rev. Lett., **45**, 566, (1980).

[26] Vosko S. H., Wilk L., Nusair M. , "Accurate spin-dependent electron liquid correlation energies for local spin density calculations: a critical analysis", Can. J. Phys., **58**, 1200, (1980).

[27] Perdew J. P. &, Wang Y. , "Accurate and simple analytic representation of the electron-gas correlation energy", Phys. Rev. B, **45**, 13244, (1992).

[28] Perdew J. P., Zunger A., "Self-interaction correction to density-functional approximations for many-electron systems", Phys. Rev. B, **23**, 5048, (1981).

[29] Becke A. D., "Perspective: Fifty years of density-functional theory in chemical physics", J. of Chem. Phys., **140**, A301, (2014) .

[30] Perdew J.P. et al., "Atoms, molecules, solids, and surfaces: Applications of the generalized gradient approximation for exchange and correlation". Phys. Rev. B, **46**, 6671, (1992).

[31] Van der Waals J.D., "Over de Continuiteit van den Gas- en Vloeistoftoestand (on the continuity of the gas and liquid state)", PhD thesis, (1873).

[32] Margenau H. & Kestner N. R. , "Theory of Interatomic Forces", 2nd ed., Pergamon Press, Oxford, 1969.

[33] Eisenshitz R. & London F. , "Über das Verhältnis der van der Waalsschen Kräfte zu den homöopolaren Bindungskräften", Z. Phys., **60**, 491 (1930).

[34] Grimme S. , "Semiempirical GGA-type density functional constructed with a long-range dispersion correction", J. Comp. Chem, **27**, 1787, (2006).

[35] Vydrov & Van Voorhis, "Nonlocal van der Waals density functional: the simpler the better", J of Chem. Phys, **133**, 244103, (2010).

[36] Grimme S. , "Accurate description of van der Waals complexes by density functional theory, including empirical corrections", J. Comp. Chem. **25**, 1463, (2004).

[37] Perdew J. P. , Burke K. , Ernzerhof M. , Phys. Rev. Lett., **77**, 3865, (1996); Erratum Phys. Rev. Lett., **78**, 1396, (1997).

[38] Csonka G. et al., "Assessing the performance of recent density functionals for bulk solids". Phys. Rev. B, **79**, 155107, (2009).

[39] Sabatini R. , Gorni T. , de GirOncoli S., "Nonlocal van der Waals Density Functional Made Simple and Efficient", Phys. Rev. B, **87**, 041108, (2013).

[40] Roman-Perez G. & J.M. Soler, "Efficient Implementation of a van der Waals Density Functional: Application to Double-Wall Carbon Nanotubes", Phys. Rev. Lett., **103**, 096102, (2009).

[41] Dion M., Rydberg H., Schröder E., Langreth D.C., Lundqvist B.I., "Van der waals density functional for general geometries", Phys. Rev. Lett., **92**, 246401, (2004).

[42] Zhang Y. & Yang W., "Comment on "generalized gradient approximation made simple"", Phys. Rev. Lett., **80**, 890, (1998)

[43] Puzder A., Dion M., Langreth D.C., "Binding energies in benzene dimers: Nonlocal density functional calculations", J. Chem. Phys., **124**, 164105, (2006).

[44] Peng Q. et al., "Van der Waals Density Functional Theory vdW-DFq for Semihard Materials", Crystals, **9**, 243, (2019).

[45] Perdew J.P. et al., "Restoring the density-gradient expansion for exchange in solids and surfaces", Phys. Rev. Lett., **100**, 136404, (2008).

[46] Hamada I., "van der waals density functional made accurate", Phys. Rev. B, **89**, 121103, (2014).

[47] Berland F. et al, "Exchange functional that tests the robustness of the plasmon description of the van der waals density functional", Phys. Rev. B, **89**, 035412, (2014).

[48] Hamann D. R., Schlüter M., Chiang C., "Norm-Conserving Pseudopotentials", Phys. Rev. Lett., **43**, 1494, (1979).

[49] Vanderbilt D., "Soft self-consistent pseudopotentials in a generalized eigenvalue formalism", Phys. Rev. B, **41**, 7892, (1990).

[50] Vanderbilt D., "Soft self-consistent pseudopotentials in a generalized eigenvalue formalism", Phys. Rev. B, **41**, 7892, (1990).

[51] Dal Corso A., "Projector augmented-wave method: Application to relativistic spin-density functional theory", Phys. Rev. B, **82**, 075116, (2019).

[52] Williams T. & Kelley C., "Gnuplot 4.5: an interactive plotting program", URL http://gnuplot.info.

[53] Kokalj A., "Computer graphics and graphical user interfaces as tools in simulations of matter at the atomic scale", Comp. Mater. Sci., **28**, 155, (2003).

[54] Wood R. M., "The Lattice Constants of High Purity Alpha Titanium", Proc. Phys. Soc., **80**, 783, (1962).

[55] Kittel C., "Introduction to Solid State Physics", 8th edition. Hoboken, NJ: John Wiley & Sons, Inc, (2005).

[56] Philipsen P.H.T. & E.J. Baerends, "Cohesive energy of $3d$ transition metals: Density functional theory atomic and bulk calculations", Phys. rev. B, **54**, 5326, (1996).

[57] https://materialsproject.org/materials/mp-77/

[58] Diéguez O. & Marzari N., "A first-principles characterization of the structure and electronic structure of α-S and Rh-S chalcogenides", Phys. Rev. B, **80**, 214115, (2009).

[59] Rettig S.J.& Trotter J., Acta Cryst., **43**, 2260, (1987).

[60] Chianelli et al., Mat. Res. Bul., **10**, 1379, (1975).

[61] Clerk D.G. et al., "Periodic Hartree-Fock Study of TiS_2", J. Phys-Chem, **100**, 15735, (1996).

[62] Beaumale M. et al., "Electron doping and phonon scattering in $Ti_{1+x}S_2$ thermoelectric compounds", Acta Mater., **78**, 86, (2014).

[63] Mainwaring D. E. et al., "Titanium sulphide nanoclusters formed within inverse micelles", Solid State Commun., **140**, 355, (2006).

[64] Dolui K. & Sanvito S., School Phys. AMBER CRANN Inst. Trinity College Dublin 2 Ireland, (2013).

[65] Fang C. M. et al., "Bulk and surface electronic structure of 1T-TiS_2 and 1T-$TiSe_2$, Phys. rev. B, **56**, 4455, (1997).

[66] Mo Y. et al., "Comparative study of semilocal density functionals on solids and surfaces", Chem. Phys. Lett., **682**, 38, (2017).